The GIEMS-MethaneCentric database: a dynamic and comprehensive global product of methane-emitting aquatic areas

Juliette Bernard[1,2], Catherine Prigent[1,3], Carlos Jimenez[3,1], Etienne Fluet-Chouinard[4], Bernhard Lehner[5], Elodie Salmon[2], Philippe Ciais[2], Zhen Zhang[6], Shushi Peng[7], and Marielle Saunois[2]

[1]LERMA, Paris Observatory, CNRS, PSL, Paris, France
[2]Laboratoire des Sciences du Climat et de l'Environnement, CEA-CNRS-UVSQ, Gif-sur-Yvette, France
[3]Estellus, Paris, France
[4]Earth System Sciences Division, Pacific Northwest National Laboratory, Richland, WA, USA
[5]Department of Geography, McGill University, Montreal, QC H3A 0B9, Canada
[6]Institute of Tibetan Plateau Research, Chinese Academy of Sciences, Beijing, China
[7]College of Urban and Environmental Sciences, Peking University, Beijing 100871, China

Correspondence: Juliette Bernard (juliette.bernard@obspm.fr) and Catherine Prigent (catherine.prigent@obspm.fr)

Abstract.

The Global Inundation Extent from Multi-Satellites (GIEMS) database first published in 2001 (Prigent et al., 2001) was a key advance toward the accurate representation of wetlands globally by providing dynamic time series of global surface water based on passive microwave observations. This study supplements the second version of GIEMS (GIEMS-2) with other datasets to produce GIEMS-MethaneCentric (GIEMS-MC), a dynamically mapped dataset of methane-emitting waterlogged and inundated ecosystems. We separated open water from wetlands in GIEMS-MC by using the Global Lakes and Wetlands Database version 2 (GLWDv2), while adding unsaturated peatland areas undetected by GIEMS-2. Rice paddies are identified using the Monthly Irrigated and Rainfed Crop Areas (MIRCA2000) product. A specific coastal zone filtering is applied to avoid ocean artifacts while preserving coastal wetlands. GIEMS-MC covers the period 1992-2020 on a monthly scale at 0.25°x0.25° spatial resolution. The GIEMS-MC product includes two layers of monthly wetland time series - one for flooded and saturated wetlands and another for all wetlands and peatlands - together with seven layers of compatible static maps of open water bodies (lakes, rivers, reservoirs) and seasonal rice paddy maps used in its production. The dominant vegetation and wetland types per pixel are also provided in GIEMS-MC variables. GIEMS-MC is compared to Wetland Area and Dynamics for Methane Modelling (WAD2M), a dataset providing dynamic wetland information. In terms of wetland extent, GIEMS-MC all wetlands and peatlands and WAD2M show similar results, with a mean annual maximum of 7.7 Mkm^2 for GIEMS-MC and 6.8 Mkm^2 for WAD2M, and similar spatial patterns in most regions. The GIEMS-MC seamless time series represents a significant advance in wetland representation for methane modelling, although limitations remain in the accurate identification of rice, coastal and peatland areas. This resource provides harmonized dynamic maps of aquatic methane emitting surfaces and is available at https://doi.org/10.5281/zenodo.13919645 (Bernard et al., 2024a).

1 Introduction

Following a stable period from 1999 to 2006, atmospheric methane levels have started to rise again, reaching a record growth rate of +18 ppb yr^{-1} in 2021 (Lan et al., 2024). This increase is a cause for concern, particularly given that anthropogenic emissions of this potent greenhouse gas account for approximately one-third of the human-induced radiative forcing (Szopa et al., 2021). As a chemically active greenhouse gas with multiple, time-varying sources and sinks (Saunois et al., 2024), closing the methane budget is challenging. The causes of the observed increase in atmospheric methane remain uncertain. Potential factors include increased human or natural emissions, reduced sinks, or a combination of these factors. However, isotopic evidence suggests that biogenic sources (livestock, wetlands, waste, etc.) may play a significant role in the observed increase (Nisbet et al., 2016, 2019).

Among the sources, natural emissions from wetlands and freshwater ecosystems account for 145 to 369 Tg CH$_4$ yr^{-1}, i.e., 25 to 51% of global methane emissions (Saunois et al., 2024). Wetland emissions show significant inter-annual variability (Bousquet et al., 2006; Bridgham et al., 2013) and are sensitive to climate (Bridgham et al., 2013; Zhang et al., 2023). Thus, better understanding natural methane emissions variability in the past will inform future predictions of wetland emissions and their feedback on climate. Large uncertainties remain for both wetlands and freshwater ecosystems methane emissions (Saunois et al., 2020; Canadell et al., 2021). This is due to the difficulty of modelling methane fluxes, which depend on many biotic and abiotic factors (Bridgham et al., 2013; Ge et al., 2024), to the small number of flux observations (Canadell et al., 2021), and to uncertainties in wetland and freshwater area (Bridgham et al., 2013; Melton et al., 2013; Saunois et al., 2020; Canadell et al., 2021), including issues of double counting, where the same area may be counted twice under different categories, inflating estimated emissions (Canadell et al., 2021; Thornton et al., 2016). Yet, the area covered by seasonal wetlands remains the single largest source of uncertainty on wetland CH$_4$ emissions (Melton et al., 2013; Peltola et al., 2019; Poulter et al., 2017; Zhang et al., 2017).

The first global wetland map was produced by Matthews and Fung (1987), providing composite static information on wetland types. Since then, new static wetland products have been established, either from composite information (Lehner and Döll, 2004; Tootchi et al., 2019; Tuanmu and Jetz, 2014) or from remote sensing approaches (Loveland et al., 2000; Friedl et al., 2002; Bartholomé and Belward, 2005; Carroll et al., 2009; Feng et al., 2016). Further datasets have been developed based on hydrological model outputs (Ringeval et al., 2012; Wania et al., 2013; Xi et al., 2022), presenting their advantages and disadvantages compared to satellite-derived products. Those models can be used both to reconstruct the historical distribution of wetlands and to predict their future evolution. Modelling can be an effective method for producing a global map of wetlands, particularly where physics-based models can reflect the mechanisms by which wetlands are formed. The two main limitations of these model outputs are 1) that hydrological models are simplified representations of the real-world complexity of wetlands (e.g., models often focus on a single water surface generation process (Obled and Zin, 2004)), and 2) that human interference is not well accounted for in the models (Hu et al., 2017). Moreover, observations are required to constrain and/or validate these model predictions.

However, there are only a few available observational dynamic time series of surface water maps at a global scale. Notably, these include: 1. the Global Inundation Extent from Multi-Satellites (GIEMS and GIEMS-2) (Prigent et al., 2001, 2007; Papa et al., 2010; Prigent et al., 2020) and its downscaled versions (Fluet-Chouinard et al., 2015; Aires et al., 2017), and 2. the Surface Water Microwave Product Series (SWAMPS) (Schroeder et al., 2015; Jensen and Mcdonald, 2019).

GIEMS-2 and SWAMPS both provide monthly fractions of surface water at 0.25°x0.25° for 1992-2020, mainly based on passive microwave observations from Special Sensor Microwave Imager (SSM/I) and the Special Sensor Microwave Imager Sounder (SSMIS). Although SWAMPS and GIEMS-2 both aim to represent both inundated surfaces and are produced using similar input data, they present significant differences both in terms of spatial distribution and inter-annual variations (Pham-Duc et al., 2017; Bernard et al., 2024b).

GIEMS-2 and SWAMPS products do not differentiate surface water categories, e.g., wetland, lake, reservoir, pond, or rice paddy, and are therefore not directly usable for wetland studies modeling seasonally inundated wetlands separately from open water bodies. Recent efforts have been made by Zhang et al. (2021b) to produce the Wetland Area and Dynamics for Methane Modeling (WAD2M) product based on SWAMPS, which represents a pioneering attempt to dynamically map wetlands, including peatlands. Using additional high-resolution static estimates of wetlands and open permanent water, as well as seasonal information on rice paddies, Zhang et al. (2021b) were able to apply these correction layers to SWAMPS to distinguish wetlands from other surface water. WAD2M version 2.0 (Zhang et al., 2021a) provides monthly estimates on a global scale for 2000-2020 at 0.25°x0.25°. However, WAD2M has encountered difficulties in capturing reliable inter-annual trends (Zhang et al., 2021b; Bernard et al., 2024b). In fact, issues in SWAMPS are propagated into WAD2M, such as ocean/desert artifacts leading to overestimation and abrupt changes in time series partly due to changes in satellites (Pham-Duc et al., 2017; Bernard et al., 2024b).

In an attempt to compare the corrected wetland extent of WAD2M and GIEMS, McNicol et al. (2023) applied the same correction layers to GIEMS-2, but this exercise did not eliminate the large differences between these two datasets. In particular, the WAD2M procedure rescales the SWAMPS surface water extent fractions, which are always positive, with other high resolution static wetland datasets, which potentially produces some unreliable seasonality where the wetland fractions in SWAMPS are below the instrumental noise level. On the contrary, GIEMS-2 shows some zero fractions over numerous pixels where no water is detected. This makes it impossible to use the same procedure as in Zhang et al. (2021b) to produce WAD2M from SWAMPS. The correction procedure needs to be modified to adapt to GIEMS-2. Furthermore, since the release of WAD2M, the most recent maps of aquatic ecosystems have been aggregated into the Global Lakes and Wetlands Database version 2 (GLWDv2), which now offers the most comprehensive and up-to-date representation of global wetland classes (Lehner et al., 2024a).

This study presents a new comprehensive database of methane emitting surfaces, named the Global Inundation Extent from Multi-Satellites-MethaneCentric (GIEMS-MC). GIEMS-MC aims at providing spatially and dynamically consistent maps of the different methane-emitting ecosystems, with the purpose of providing data for modelling methane emissions at the global scale (0.25°x0.25°) over 1992-2020. In particular, two time series of wetland maps are developed at monthly timescale: inundated and saturated wetlands (ISW), and all wetlands including non-inundated peatlands (inundated and saturated wetlands

+ peatlands, ISW+P). GIEMS-MC also provides compatible information from the ancillary data used, including static surface extents of open permanent waters (lakes, rivers, reservoirs, estuaries, deltas), and seasonal surface extents of rice paddies, along with dominant vegetation on wetland classes. GIEMS-MC takes advantage of the GIEMS-2 product that offers ∼30-year seamless time series of surface water with realistic seasonality and inter-annuality (Prigent et al., 2020; Bernard et al., 2024b), and largely benefits from the recently developed comprehensive static map of GLWDv2 (Lehner et al., 2024a). This article outlines the methodology behind the production of GIEMS-MC and provides an analysis and comparison with existing datasets : WAD2M (Zhang et al., 2021b), GLWDv2 (Lehner et al., 2024a), and the original GIEMS-2 (Prigent et al., 2020). Two inundation products based on Cyclone Global Navigation Satellite System (CYGNSS) data are also used for comparison over the Sudd (Zeiger et al., 2023; Gerlein-Safdi et al., 2021). The sensitivity of the wetland estimates to the different process steps is also discussed.

2 Datasets

This section presents the three types of data used in the production of GIEMS-MC: 1. the surface data of the different aquatic ecosystems, 2. the data used for the masks and additional ecosystem layers, and 3. the WAD2M comparison dataset.

2.1 Input datasets to GIEMS-MC (GIEMS-2, GLWDv2, MIRCA2000)

The GIEMS-2 dataset, spanning 1992 to 2015 and extended to 2020 in this study, provides monthly global maps of surface water extent with a spatial resolution of 0.25°x0.25° (Prigent et al., 2020). GIEMS-2 includes all continental water surfaces, such as wetlands, rice paddies, rivers, reservoirs, and lakes, but excludes large lakes (> 15 000 km^2). The original GIEMS-1 methodology (Prigent et al., 2001, 2007; Papa et al., 2006; Prigent et al., 2007; Papa et al., 2008, 2010) and the GIEMS-2 algorithm (Prigent et al., 2020; Bernard et al., 2024b) have been extensively evaluated against other observational products, demonstrating robust capture of seasonal and inter-annual variability, despite uncertainties in wetland extent between currently available products. GIEMS-2 relies primarily on inter-calibrated passive microwave observations from the SSM/I and SSMIS satellites (Fennig et al., 2020) at frequencies from 19 to 85 GHz. The microwave signal is influenced by atmospheric conditions (e.g., water vapor, clouds) and surface variables (e.g., surface temperature, vegetation, snow) by ancillary information other to limit these artifacts, as described in Prigent et al. (2020). Microwave observations are complemented by other satellite information to limit these artifacts, as described in Prigent et al. (2020). Specifically, active microwave satellite data and Normalised Difference Vegetation Index (NDVI) derived from visible and near-infrared measurements are used to characterize vegetation and mitigate its influence on the passive microwave signal. Since snow contamination prevents the calculation of surface water, snow-covered pixels (as defined by meteorological reanalysis), are assigned a water fraction of 0 in the previous studies and in the distributed GIEMS-2 product. Passive microwaves are sensitive to the presence of water, including estuarine and offshore marine waters. To avoid misinterpretation of the data, coastal pixels were filtered out in the distributed GIEMS-2 product, leading to a possible underestimation of inundated surface extent in the coastal areas. Here we use an unfiltered version

of GIEMS-2 in which coastal regions are not excluded, in order to improve the coastal cleaning process during the production of GIEMS-MC based on GLWDv2, as described in Sect. 3.

The Global Lakes and Wetlands Database version 2 (GLWDv2) (Lehner et al., 2024a) provides comprehensive global maps of aquatic ecosystems synthesized from a variety of ground- and satellite-based data products. GLWDv2 combines various data products to generate consolidated and harmonized static maps representative of the period 1990-2020. The GLWDv2 product contains 33 wetland and water body classes, which are listed in Supplementary Table S1. GLWDv2 represents the maximum extent of each of its 33 classes (in pixel fraction) at a resolution of 15 arc seconds (approximately 500 m at the equator). For this study, the 33 GLWDv2 class maps were aggregated at 0.25°x0.25°.

Rice cultivation varies seasonally according to cropping calendars, and their inundated cover can be confused with that of wetlands. The majority of global rice paddy maps are static representations, typically for a specific time period. A notable data source that gives insights into the seasonality of rice paddy at global scale is the MIRCA2000 dataset (Portmann et al., 2010). MIRCA2000 provides data on irrigated and rainfed cultivated areas at a resolution of 5 arc minutes for each month of a reference year (representative of circa 2000). The dataset integrates several data sources, including agricultural statistics such as cropping calendar and remote sensing data. This study uses both irrigated and rainfed rice data extracted from the MIRCA2000 dataset.

2.2 Ancillary and correction datasets (ERA5, ESA CCI)

The European Centre for Medium-range Weather Forecasts reanalysis (ECMWF-ERA5) (Hersbach et al., 2020) is a state-of-the-art reanalysis for climate applications. It provides global climate and weather data spanning from 1940 to the present. ERA-5 uses assimilation techniques by integrating a wide diversity of observational data to deliver hourly estimates of multiple atmospheric, land, and oceanic variables at a resolution of 31 km. ERA5 can be downloaded at a resolution of 0.25° x 0.25° from https://cds.climate.copernicus.eu/. In the GIEMS-2 and GIEMS-MC process, the area covered with snow in a pixel is derived from the ERA5 variables snow density and snow depth.

The European Space Agency (ESA) Climate Change Initiative (CCI) Land Cover dataset (ESA, 2017) provides a classification of land cover features at a spatial resolution of 300 m for each year from 1992 to 2022. The dataset is derived from various satellite Earth observation data. According to the standards of the United Nations Land Cover Classification System (Di Gregorio and Jansen, 2005), it contains 22 land cover classes (Supplementary Table S2), including 18 vegetation categories and urban, bare, water bodies, and snow/ice categories. The ESA CCI Land Cover dataset can be accessed via the ESA CCI Land Cover project website : https://maps.elie.ucl.ac.be/CCI/viewer/download.php. Here, we aggregated a version to 0.25° x 0.25°, where the dominant class within each pixel is determined based on the highest fractional coverage.

2.3 Comparison dataset (WAD2M)

The Wetland Area and Dynamics for Methane Modeling (WAD2M) version 2.0 dataset (Zhang et al., 2021a, b) is a comprehensive global product designed to support methane modelling. It provides the fraction of wetland area, including peatlands, at a resolution of 0.25°x0.25°, and at a monthly time step for 2000-2020. The WAD2M dataset uses dynamic data from the Sur-

face Water Microwave Product Series (SWAMPS) dataset (Jensen and Mcdonald, 2019), which provides monthly inundation fraction at 0.25°x0.25°. Similar to GIEMS-2, SWAMPS is derived mainly from passive microwave observations from SSM/I and SSMIS, but the methodology and ancillary data used differ between the two products (Schroeder et al., 2015; Prigent et al., 2020), resulting in important differences in some regions (Pham-Duc et al., 2017; Bernard et al., 2024b). The creation of WAD2M involved combining SWAMPS surface inundation time series with static datasets to distinguish between different wetland types. The static datasets used in WAD2M production are 4 peatlands maps (NCSCD from Hugelius et al. (2013), CAWASAR from Widhalm et al. (2015), GLWDv1 from Lehner and Döll (2004), and CIFOR from Gumbricht et al. (2017)), one inland open water map (GSW from Pekel et al. (2016)), one coastal mask (MOD44W from Carroll et al. (2009)), and seasonal irrigated rice map (MIRCA2000 from Portmann et al. (2010)). These static layers allow the wetland fractions to be rescaled to include non-inundated wetlands (peatlands) and exclude non-wetland inundated areas (irrigated rice paddies and open waters).

3 Methods

3.1 Overview of the methodology

GIEMS-2 uses satellite passive microwave data, which are particularly responsive to the presence of water, to determine the fraction of inundated and saturated soil per pixel. However, modifications to the GIEMS-2 dataset are required in order to remove inundated or saturated areas that are not wetlands (e.g., rice paddies, lakes, rivers, reservoirs), and to add wetlands where the water table may be undetectable below ground level (e.g., some peatlands). As a consequence of the aforementioned remote sensing approach, the present study will first distinguish the inundated wetlands identified by GIEMS-2 and then add the unsaturated wetlands. In addition to GIEMS-2, the GLWDv2 dataset will be used.

The original GIEMS-2 product (Prigent et al., 2020) has been extended to 2020 (Bernard et al., 2024b), and a special version without coastal filtering is used here. In total, seven steps, described in the following subsections, are required to derive wetland maps from this data. The operations are made in terms of pixel fraction f on a regular grid of 0.25°x0.25°. Multiplication by pixel area is then needed to derive wetland extent. A summary of the procedure is shown in Fig. 1, and the seven steps are described in detail in the following subsections.

3.1.1 Applying ocean mask

For consistency with GLWDv2, we here used the regional shapefiles of the HydroATLAS database (version 1.0; Linke et al. (2019)), which provides near-identical coastlines as GLWDv2. This allowed us to calculate the ocean fraction for each 0.25° x 0.25° pixel. The ocean water fraction is set to -999 if the ocean fraction of a pixel is greater than 99%, to avoid confusion between ocean pixels and pixels where no surface water was detected (zero fraction pixels).
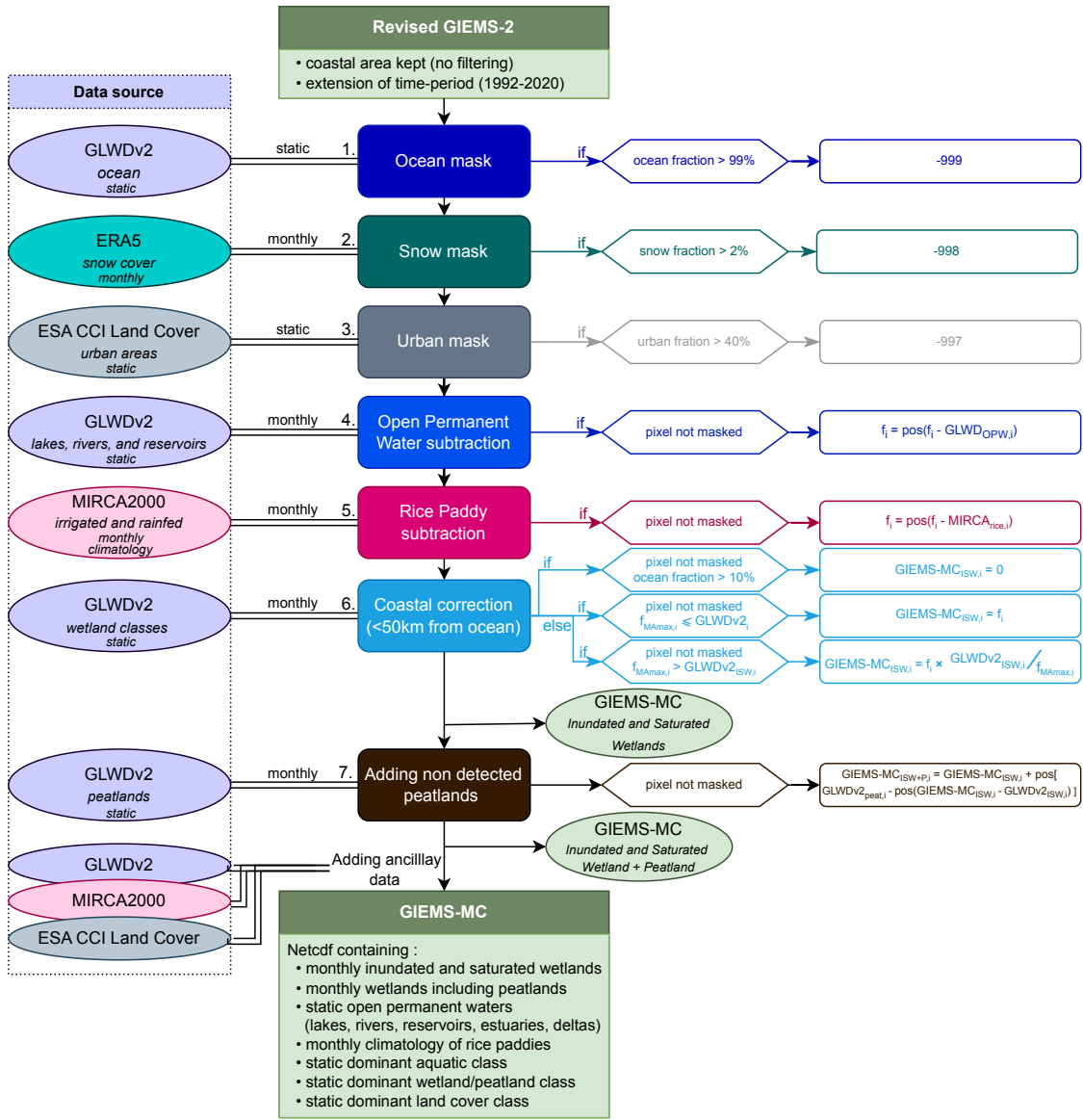
Figure 1. Schematic of the GIEMS-MC dataset production process. All operations are performed in terms of pixel fractions at a resolution of 0.25°x0.25°. Ocean pixels are set to -999, snow-covered pixels are set to -998, and urban pixels are set to -997 in a revised version of GIEMS-2. Open permanent water and then rice paddies areas are subtracted from the surface water areas. A specific coastal cleaning is applied to remove ocean contamination, resulting in a dynamic map of Inundated and Saturated Wetland (GIEMS-MC$_{ISW}$). Peatlands areas undetected by GIEMS-2 are added to derive a dynamic map of all wetlands including peatlands, called Inundated and Saturated Wetland + Peatland (GIEMS-MC$_{ISW+P}$). Finally, initial ancillary data information is added to the product so that users can easily access the different fraction maps of all surface water categories, including Inundated and Saturated Wetland, Inundated and Saturated Wetland + Peatland, open permanent waters, rice paddies, and the dominant wetland and vegetation classes. f_i refers to the fraction of a pixel i before the corresponding step. pos(f) refers to the positive part of f, i.e. pos(f) = max(f,0). GLWDv2 Open Permanent Water (GLWDv2$_{OPW}$) is the sum of all GLWDv2 classes 1 to 5 and 30. GLWDv2 Inundated and Saturated Wetland (GLWDv2$_{ISW}$) is the sum of all GLWDv2 wetlands excluding peatlands corresponding to classes 8 to 21, 28, 29, 31, and 32. GLWDv2 Peatland (GLWDv2$_{peat}$) is the sum of all GLWDv2 peatlands corresponding to classes 22 to 27.

3.1.2 Applying snow mask

GIEMS-2 surface water detection relies primarily on passive microwave observations, which are affected by the presence of snow (Foster et al., 1984). Thus, the surface water fraction cannot be reliably quantified in the presence of snow. Consequently, the surface water detection algorithm in the GIEMS-2 production is not run when snow is present in a pixel. To exclude these snow-covered pixels, ECMWF snow information from ERA5 is used in the GIEMS-2 processing, and pixels with a snow fraction above 2% are set to a surface water fraction of 0 (Prigent et al., 2020). In GIEMS-MC, the pixel value is given its dedicated snow flag value of -998 when the snow fraction of a pixel is greater than 2%. It should be noted that this mask remains for all subsequent steps and is therefore also applied to the peatlands (step 7).

3.1.3 Applying urban mask

It has been observed that unexpectedly large water surfaces are detected by GIEMS-2 in areas of high urban density. This could be due to the different surface materials used in buildings, some of which strongly reflect microwaves. For example, highly reflective areas over Paris are misinterpreted as water due to predominance of zinc roofs. To apply an urban mask, the urban class product of the ESA CCI land cover map aggregated at 0.25°x0.25° is used. The grid cells with urban percentage above 40% are systematically masked to -997 to avoid any confusion between urban and water surfaces. Note that applying this urban mask results in neglecting change in terms of surface water global area (<1% change on mean extent), but this avoids local artifacts over the high urban density areas.

3.1.4 Subtracting open permanent waters

Inland permanent open waters are considered separately from wetlands in methane budgets (Saunois et al., 2020; Canadell et al., 2021), as different methane production and transport processes are involved. To derive wetland maps, these open permanent surface water areas must be subtracted from the GIEMS-2 estimates. Here, we define permanent open water as non-vegetated, permanently inundated areas that are not wetland. Some dynamic datasets could have been used, but consistency was preferred, so GLWDv2 harmonized maps were used in GIEMS-MC production. Then, permanent open water areas of GLWDv2 corresponding to layers 1 to 5 and 30 (*Freshwater Lake*, *Salt Lake*, *Reservoir*, *Large River*, *Large Estuarine River* and *Large River Delta*) are subtracted from the GIEMS-2 fractions. These GLWDv2 areas are derived from HydroLAKES (Messager et al. (2016) ; Lakes), the Global Dam Watch (GDWv1) database (Lehner et al. (2024b) ; Reservoirs), the Global River Width from Landsat (GRWL) dataset (Allen and Pavelsky (2018) ; Large Rivers) and augmented with the Global Surface Water (GSW) database (Pekel et al., 2016)). Note that the floodplain ecosystems are included in other GLWDv2 classes (10 to 15) and are therefore retained in GIEMS-2 when constructing GIEMS-MC.

3.1.5 Subtracting rice paddies

Rice paddies are intermittently saturated or inundated depending on irrigation practices, and their methane emissions are considered to be an anthropogenic source that should be separated from those of natural wetlands. GLWDv2 contains a static

rice paddy map, but the seasonal variation of rice paddies is important in terms of extent and needs to be taken into account to avoid over-subtraction of rice paddies in the GIEMS-MC process. However, there is to our knowledge no dynamic (intra-annual resolution) product available that represents rice paddies at global scale over our observation period. As the MIRCA2000

215   product provides maps with a typical seasonality (circa 2000) of global rice paddies, it appears to be the most appropriate product available. Consequently, the MIRCA2000 12-month seasonality of irrigated and rainfed rice paddy areas is subtracted from the area estimates. This rice paddy processing and its uncertainties are discussed further in Sect. 5.2.2.

3.1.6 Correcting ocean contamination

The GIEMS-2 version used here has not been filtered in coastal areas, as it is usually done in the distributed GIEMS-2 version.

220   The SSM/I and SSMIS passive microwave observations used in GIEMS-2 production are very sensitive to the presence of water, including the ocean. The GIEMS-2 fraction and seasonality estimates are less reliable for pixels with larger ocean fractions. Thus, pixels containing more than 10% ocean in GLWDv2 ($GLWDv2_{ocean} > 10\%$) are set to 0. Tests were made to tune this 10% threshold, to avoid masking all pixels containing a small fraction of ocean area, while ensuring reasonable seasonality. However, pixels containing up to 10% ocean area will undergo an additional coastal cleaning procedure that follows. Ocean

225   contamination can arise from the presence of ocean within the pixel, but also from the ocean in neighboring pixels. A GIEMS-2 pixel (~ 800 km^2 at the equator, ~ 400 km^2 at 60°N or S) is smaller than the -3dB footprint of the original microwave satellite observations (69 km×43 km at 19 GHz and 37 km×28 km at 37 GHz). Moreover, microwave energy is also measured in the side lobes of the satellite instrument footprint. Coastal areas should then undergo a cleaning process to reduce these artifacts. Pixels whose centers are between 0 and 50 km from a coastline or large lakes (> 15 000 km^2) are considered as coastal areas.

230   In an attempt to correct for ocean contamination, the following procedure is applied to ensure that the wetland areas in GIEMS-MC in coastal regions are equal to or lower than the GLWDv2 inventory. This is done by calculating GLWDv2 Inundated and Saturated Wetland ($GLWDv2_{ISW}$), i.e., the sum of all GLWDv2 wetlands excluding peatlands (which are not necessarily saturated surface water) corresponding to classes 8 to 21, 28, 29, 31, and 32. The fraction of the modified version of GIEMS-2 up to this step, incorporating the 5 aforementioned corrections and cleaning processes (ocean, snow, urban masks and

235   open water, and rice paddies removal), is called f. Its Mean Annual Maximum f_{MAmax} is calculated by taking a monthly average over all years and taking the maximum of this monthly seasonality for each pixel i. In the coastal region, for each time step and for each pixel i, with the resulting areas called Inundated and Saturated Wetland map in GIEMS-MC ($GIEMS-MC_{ISW}$):

- if $GLWDv2_{ocean, i} > 10\%$:
  then $GIEMS-MC_{ISW, i} = 0$

240   - if $GLWDv2_{ocean, i} \leq 10\%$ and $f_{MAmax, i} < GLWDv2_{ISW, i}$:
  then $GIEMS-MC_{ISW, i} = f_i$

- if $GLWDv2_{ocean, i} \leq 10\%$ and $f_{MAmax, i} > GLWDv2_{ISW, i}$:
  then $GIEMS-MC_{ISW, i} = f_i * \frac{GLWDv2_{ISW, i}}{f_{MAmax, i}}$

3.1.7 Adding peatlands

Finally, in order to have a complete map of wetlands, the peatlands not detected by GIEMS-2 (monthly unsaturated or unflooded peatlands) have to be taken into account in the wetland fraction. This is done using the following procedure. The sum of GLWDv2 peatlands, i.e. GLWDv2 classes 22 to 27, is denoted here as $GLWDv2_{peat}$. GLWDv2 peatland information is a composite product relying on most up-to-date peatland maps : PeatMap (Xu et al. (2018), global), SoilGrids250m (Hengl et al. (2017), global), Northern Peatlands (Hugelius and Olefeldt, north of 23° N), and CIFOR (Gumbricht et al. (2017), only south of 23.5° N). More details can be found in Lehner et al. (2024a). $GLWDv2_{peat}$ represents 4.26 Mkm^2, which is consistent with primary PeatMap estimates of 4.23 Mkm^2. The peatlands detected by GIEMS-2 are derived by the difference, if positive, between $GIEMS-MC_{ISW}$ and $GLWDv2_{ISW}$. The undetected peatlands are then derived for each month as the difference between $GLWDv2_{peat}$ and the peatlands detected by GIEMS-2. These undetected peatlands are added to the $GIEMS-MC_{ISW}$, resulting in GIEMS-MC Inundated and Saturated Wetland + Peatland ($GIEMS-MC_{ISW+P}$), i.e., for each pixel i :

$$\text{undetected peatlands}_i = pos[GLWDv2_{peat\,i} - pos(GIEMS-MC_{ISW\,i} - GLWDv2_{ISW\,i})]$$
$$GIEMS-MC_{ISW+P} = GIEMS-MC_{ISW} + \text{undetected peatlands}.$$

The uncertainty in terms of areas of this step is discussed in Sect. 5.2.3.

3.2 Comparison

$GIEMS-MC_{ISW}$ is compared with the original GIEMS-2 product and $GLWD_{ISW}$. $GIEMS-MC_{ISW+P}$ is compared to $GLWDv2_{ISW+P}$ ($GLWDv2_{ISW}$ + $GLWDv2_{peat}$) and to WAD2M, as all also include peatlands (Table 3, Fig.2, and Supplementary Fig.S1). As GLWDv2 is a static map representing long term maximum extent, the GIEMS-MC Long Term maximum (LTmax) will be used for comparison with GLWDv2 instead of MAmax (Table 3). To derive this LTmax, the maximum of each pixel over the whole time period is selected. This can lead to the selection of extreme values with moderate reliability, and LTmax should then be interpreted with caution.

3.3 Description of GIEMS-MC dataset

Following the seven steps outlined, a netcdf product at 0.25°x0.25° resolution containing the derived variables and ancillary variables is created. The variables included in this product are detailed in Table 1. Its components include both dynamic monthly maps of $GIEMS-MC_{ISW}$ and $GIEMS-MC_{ISW+P}$. Permanent Open Water classes (GLWDv2), i.e., Freshwater Lake, Saline Lake, Reservoir, River, Large Estuarine River, and Large River Delta, are also added as static variables in GIEMS-MC. The 12-month seasonality of Irrigated and Rainfed Rice Paddy (MIRCA2000) is included. Three static maps provide information on the main ecosystems per pixel : the dominant aquatic class (GLWDv2), the dominant wetland or peatland class (GLWDv2), and the dominant land cover class (ESA CCI Land Cover map). This vegetation information is added in GIEMS-MC as it is expected to help improve the estimation of wetland methane emissions (Pangala et al., 2017; Vroom et al., 2022; Feron et al., 2024; Girkin et al., 2025; Ge et al., 2024).

GIEMS-MC variable	Long name	Type	Primary or main data source	Time resolution
`inund_sat_wetland_frac`	Inundated and Saturated Wetland	fraction	GIEMS-2	monthly
`inund_sat_peat_wetland_frac`	Inundated and Saturated Wetland + Peatland	fraction	GIEMS-2 + GLWDv2	monthly
`fresh_lake_frac`	Freshwater Lake	fraction	GLWDv2	static
`saline_lake_frac`	Saline Lake	fraction	GLWDv2	static
`reservoir_frac`	Reservoir	fraction	GLWDv2	static
`river_frac`	Large River	fraction	GLWDv2	static
`estu_river_frac`	Large Estuarine River	fraction	GLWDv2	static
`delta_frac`	Large River Delta	fraction	GLWDv2	static
`rice_irri_frac`	Irrigated Rice Paddy	fraction	MIRCA2000	12-month seasonality
`rice_rainfed_frac`	Rainfed Rice Paddy	fraction	MIRCA2000	12-month seasonality
`dom_aqua_class`	Dominant Aquatic Class	33 classes (Table S1)	GLWDv2	static
`dom_wet_peat_class`	Dominant Wetland or Peatland Class	25 classes (Table S1)	GLWDv2	static
`dom_land_cover_class`	Dominant Land Cover Class	37 classes (Table S2)	ESA CCI Land Cover	static

Table 1. Summary of GIEMS-MC variables with corresponding data sources and temporal resolution. For details about data sources, see Sect. 2 or Prient et al. (2020) for GIEMS-2, Lehner et al. (2024a) for GLWDv2, Portmann et al. (2010) for MIRCA2000, and ESA (2017) for ESA CCI Land Cover.

275 ## 4 GIEMS-MC results

4.1 Global inland water areas

To quantify the variations in terms of extent, the Mean Annual maximum (MAmax), Mean Annual mean (MAmean), and Mean Annual minimum (MAmin) are calculated by averaging the 29 years of data (21 years for WAD2M) to a typical 12-month seasonality for each pixel. Then, the maximum, the mean, and the minimum are respectively selected for each pixel.

280 Spatial correlation is defined as the pixel-by-pixel correlation between two maps, considering a specific unmasked region.

Globally, GIEMS-MC$_{ISW}$ represent 3.80 Mkm^2, with a MAmean of 1.23 Mkm^2 (Table 2). The addition of peatlands greatly increases these global areas, with GIEMS-MC$_{ISW+P}$ reaching 7.75 Mkm^2 (+3.95 Mkm^2) in terms of MAmax and 3.54 Mkm^2 (+2.27 Mkm^2) in terms of MAmean. This increase is mainly due to Europe+Siberia, and North America, where large peatlands contribute significantly to the total wetland area (74% and 58% respectively).

		Global	Africa	Asia	Europe +Siberia	Oceania	North America	South America
GIEMS-MC$_{ISW}$ **(Inundated and Saturated Wetland)**	MAmax	3796	515	972	616	207	827	207
	MAmean	1227	163	252	154	103	258	294
	MAmin	251	46	29	11	46	30	85
GIEMS-MC$_{ISW+P}$ **(Inundated and Saturated Wetland + Peatland)**	MAmax	7745	636	1153	2369	522	1985	1001
	MAmean	3500	295	382	888	429	790	654
	MAmin	1308	182	96	79	377	76	449
Freshwater lake	static	2045	197	76	429	22	1214	81
Saline lake	static	359	33	97	88	40	21	20
Reservoir	static	316	40	62	71	6	87	47
River	static	384	40	72	109	13	53	93
Large estuarine river	static	79	5	12	16	9	10	13
Large river delta	static	280	18	139	15	0	35	57
Irrigated Rice Paddy	MAmax	639	14	509	16	46	14	22
	MAmean	431	8	355	6	30	8	10
	MAmin	64	0	62	0	0	0	0
Rainfed Rice Paddy	MAmax	614	42	452	0	71	3	25
	MAmean	251	21	178	0	29	1	12
	MAmin	1	0	0	0	0	0	0
Total	MAmax	12271	1013	2495	3102	731	3400	1326
Total distribution	MAmax	100%	8.3%	20.3%	25.3%	6.0%	27.7%	10.8%

Table 2. Global and continental surfaces of GIEMS-MC variables in 10^3 km^2. For dynamic classes, MAmax and MAmin are shown. Total MAmax is the sum of GIEMS-MC Inundated and Saturated Wetland + Peatland MAmax, open permanent water (Freshwater Lake, Saline Lake, Reservoir, River, Large Estuarine River, Large River Delta) from GLWDv2, and Rice Paddy from MIRCA2000 MAmax (Irrigated and Rainfed). Regions correspond to the shapefiles of HydroATLAS database (version 1.0; Linke et al. (2019)).

285   GIEMS-MC$_{ISW}$ consistently shows much lower extent than the original GIEMS-2 (MAmax reduced from 6.80 Mkm^2 to 3.80 Mkm^2) that comprises all inundated and saturated areas, including non-wetland categories. The lower areas in GIEMS-MC$_{ISW}$ is mainly due to the removal of open permanent waters in Europe, Siberia, and North America, and to rice paddies subtraction in Asia. The LTmax of GIEMS-MC$_{ISW}$ reaches 8.77 Mkm^2, close to the GLWDv2$_{ISW}$ estimates of 8.22 Mkm^2.

Globally, the MAmean estimates of GIEMS-MC$_{ISW+P}$ and WAD2M are in agreement (resp. MAmean of 3.50 Mkm^2 and
4.21 Mkm^2), and the two datasets show a spatial correlation coefficient of 0.61 for MAmax over submerged land. How-
ever, regional differences exist in Africa (MAmean of 295 and 719 10^{3}km^2, respectively) and Oceania (MAmean of 429 and
572 10^{3}km^2, respectively). In those regions, WAD2M detects comparatively more water, likely due to desert contamination
in the SWAMPS product used in the WAD2M production (see Fig.2 and Supplementary Fig.S1). In Asia, Europe, Siberia,
and North America, GIEMS-MC$_{ISW+P}$ shows similar MAmean areas but has a larger MAmax-MAmin amplitude, possibly
due to 1) higher peatland estimates in GLWDv2 than in the ancillary data used in WAD2M production, which could explain
the higher MAmax, and 2) more stringent snow and coastal filtering in GIEMS-MC, which could explain the lower MAmin.
As GLWDv2 peatlands are used to derive GIEMS-MC$_{ISW+P}$ from GIEMS-MC$_{ISW}$, similar total extents are consistently found
between GIEMS-MC$_{ISW+P}$ LTmax of 12.25 Mkm^2 and GLWDv2$_{ISW+P}$ LTmax of 12.49 Mkm^2.

		Global	Africa	Asia	Europe +Siberia	Oceania	North America	South America
GIEMS-MC$_{ISW}$ (Inundated and Saturated Wetland)	LTmax	8766	1409	2097	1548	648	1594	1465
	MAmax	3796	515	972	616	207	827	207
	MAmean	1227	163	252	154	103	258	294
	MAmin	251	46	29	11	46	30	85
Orginal GIEMS-2	MAmax	6796	631	1793	1071	339	1804	945
	MAmean	2730	236	659	339	216	647	506
	MAmin	795	88	149	42	133	93	218
GLWDv2$_{ISW}$ (Inundated and Saturated Wetland)	static	8223	1010	1958	1416	541	1755	1269
GIEMS-MC$_{ISW+P}$ (Inundated and Saturated Wetland + Peatland)	LTmax	12251	1512	2242	3115	915	2628	1760
	MAmax	7745	636	1153	2369	522	1985	1001
	MAmean	3500	295	382	888	429	790	654
	MAmin	1308	182	96	79	377	76	449
WAD2M	MAmax	6756	1077	743	1675	678	1308	985
	MAmean	4208	719	370	776	572	760	778
	MAmin	2437	479	184	176	482	293	639
GLWDv2$_{ISW+P}$ (Inundated and Saturated Wetland + Peatland)	static	12486	1147	2156	3280	878	3023	1646

Table 3. Comparison of GIEMS-MC$_{ISW}$ and GIEMS-MC$_{ISW+P}$ surface extents with WAD2M (Zhang et al., 2021b) and GLWDv2 (Lehner et al., 2024a) datasets, in 10^3 km^2. For dynamic classes, MAmax and MAmin are shown. GLWDv2$_{ISW}$ refers to the sum of GLWDv2 classes 8 to 21, 28, 29, 31, and 32, while GLWDv2$_{ISW+P}$ refers to the sum of GLWDv2 classes 8 to 29, 31 and 32. Regions correspond to the shapefiles of HydroATLAS database (version 1.0; Linke et al. (2019)).
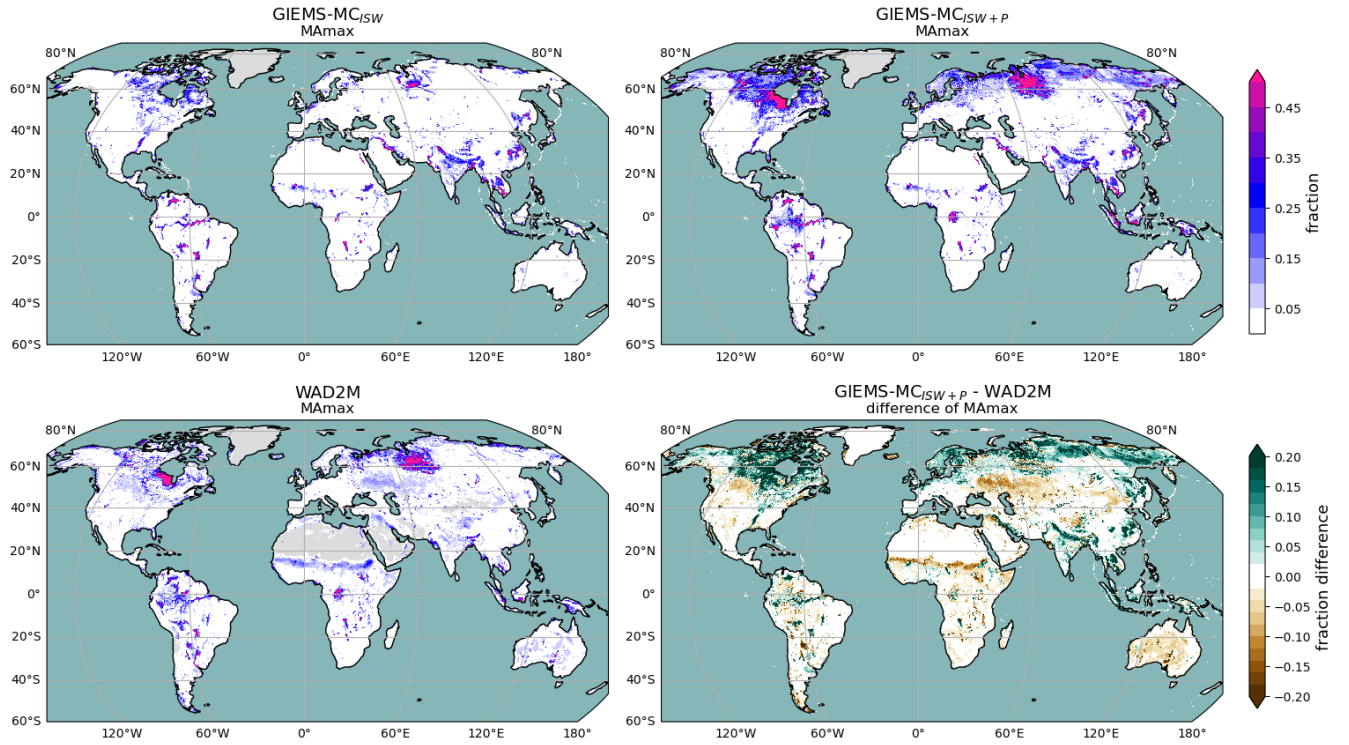
Figure 2. Global distribution of the MAmax of GIEMS-MC$_{ISW}$, GIEMS-MC$_{ISW+P}$, and WAD2M (Zhang et al., 2021b), as well as the difference of MAmax from GIEMS-MC$_{ISW+P}$ and WAD2M. Refer to Supplementary Fig. S1 for maps with MAmin.

Figure 3 provides the latitudinal distribution of a) GIEMS-MC variables and b) GIEMS-MC$_{ISW+P}$ against WAD2M. GIEMS-

300 MC$_{ISW}$ shows a relatively uniform distribution across all latitudinal zones, with a peak just south of the equator due to the Amazon basin. The inclusion of peatlands in GIEMS-MC$_{ISW+P}$ increases largely the wetland area in the boreal (>55°N, e.g., the Hudson Bay and the Siberian Low Lands) and tropical (10°S-5°N, e.g., the Congo) bands, leading to a similar distribution as in WAD2M (Fig. 2 and 3.c). Differences between GIEMS-MC$_{ISW+P}$ and WAD2M are observed around 15°N and 10-30°S, due to discrepancies between the SWAMPS and GIEMS-2 methodologies (Pham-Duc et al., 2017; Bernard et al., 2024b),

305 mostly related to desert contamination in SWAMPS (Sahel and Australia on Fig. 2).
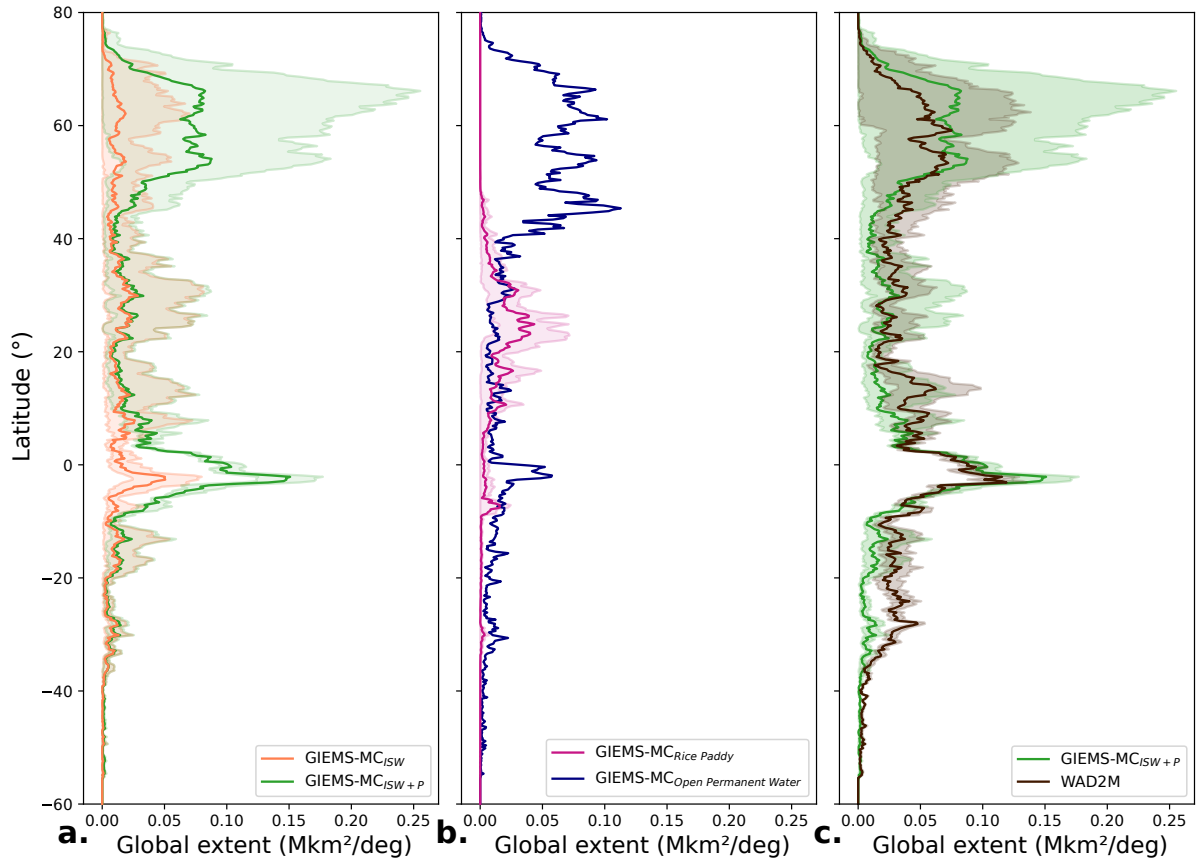
Figure 3. Latitudinal distributions of **a.** the GIEMS-MC wetland variables (Inundated and Saturated Wetlands, Inundated and Saturated Wetlands + Peatlands), **b.** GIEMS-MC wetland ancillary variables (Rice Paddy, and the sum of Open Permanent Water), and **c.** GIEMS-MC$_{ISW+P}$ and WAD2M product. For dynamic variables, solid lines represent the MAmean, while colored fillings represent the MAmax-MAmin interval. The extents are given per 1-degree latitudinal bin. The metrics (MAmin, MAmean, and MAmax) are calculated over the entire product availability period, i.e., from 1992 to 2020 for the GIEMS-MC variables and from 2000 to 2020 for WAD2M.

4.2 Regional spatial patterns over main basins

GIEMS-MC$_{ISW}$ and GIEMS-MC$_{ISW+P}$ data are analyzed in the following sections over large wetland complexes representing different environments : the Siberian Lowlands, the Sudd, the Amazon and South-East Asia.

As expected, peatland addition noticeably amplifies the extent between GIEMS-MC$_{ISW}$ (MAmax of 0.19 Mkm^2) and GIEMS-MC$_{ISW+P}$ (MAmax of 0.70 Mkm^2) over the Ob basin (Western Siberian Low Lands, Fig. 4). WAD2M and GIEMS-MC$_{ISW+P}$ consistently present similar patterns for MAmax (spatial correlation coefficient of 0.80). However, discrepancies occur in the southern part of the Ob basin that can be attributed to different snow filtering between SWAMPS (used for WAD2M) and GIEMS-2 (used for GIEMS-MC). The Boreal-Arctic Wetland and Lake Dataset (BAWLD) is also shown for

comparison (Fig. 4), as it covers the upper part of the basin (Olefeldt et al., 2021b, a). The BAWLD wetland fraction, including

315 peatland classes, exhibits patterns similar to GIEMS-MC$_{ISW+P}$ MAmax, with a spatial correlation coefficient of 0.74. BAWLD covers a slightly larger area (+6%) compared to GIEMS-MC$_{ISW+P}$ MAmax when comparing the common area covered by the two datasets.

In the Sudd basin shown in Fig. 5, GIEMS-MC$_{ISW+P}$ extent corresponds essentially to GIEMS-MC$_{ISW}$, indicating minimal presence of peatlands. For comparison, two surface water extent products, both derived from Cyclone Global Navigation

320 Satellite System L-band remote sensing observations, are also shown (Zeiger et al., 2023; Gerlein-Safdi et al., 2021). Gerlein-Safdi et al. (2021) estimates are available for the southern part of the basin (MAmax of 0.27 Mkm^2 for 2018-2019), and are much higher than the GIEMS-MC (MAmax of 0.04 Mkm^2 for 2018-2019) and WAD2M (MAmax of 0.1 Mkm^2 for 2018-2019) estimates. Zeiger et al. (2023) product provides an MAmax of 0.06 over 2018-Aug to 2019-Jul, which is within the GIEMS-MC and WAD2M estimates. While good agreement is observed in the southern part of the basin between the spatial pattern

325 of GIEMS-MC$_{ISW+P}$, WAD2M, and the product of Zeiger et al. (2023), significant disparities emerge between WAD2M and the two products in the northern-east desert region of the Sudd basin, probably due to contamination in the original SWAMPS dataset.

Over the Amazon (Fig. 6), GIEMS-MC$_{ISW}$ fractions are high (>0.5) along the main river channel, while including peatlands adds smaller surfaces along smaller secondary channels, resulting in finer spatial patterns and higher MAmax (0.31 to

330 0.56 Mkm^2). The resulting GIEMS-MC$_{ISW+P}$ MAmax map closely resembles that of WAD2M (spatial correlation coefficient of 0.77), with a slightly higher MAmax for WAD2M (0.47 Mkm^2). GIEMS-MC$_{ISW}$ and GIEMS-MC$_{ISW+P}$ extents can be potentially underestimated in this basin, as Fleischmann et al. (2022) found that GIEMS-2 estimates of inundation were likely slightly underestimated compared to higher resolution remote sensing estimates based on Synthetic Aperture Radar (SAR), with Chapman et al. (2015) finding +4% and Rosenqvist et al. (2020) +36% compared to GIEMS-2 long term maximum

335 inundation.

GIEMS-MC$_{ISW+P}$ and WAD2M agree well in South-East Asia (Fig. 7, and MAmax spatial correlation coefficient of 0.67), with GIEMS-MC$_{ISW+P}$ showing greater peatland extent than WAD2M due to higher peatland areas estimated by GLWDv2 used in GIEMS-MC production than the earlier estimates used in WAD2M.

These findings underline the legacy of the two original microwave-based datasets (GIEMS-2 and SWAMPS) used respec-

340 tively in GIEMS-MC and WAD2M production, despite the corrections. Indeed, methodological disparities between GIEMS-2 and SWAMPS production may lead to distinct spatial inundation detection patterns, particularly in regions where contamination from ocean, desert, and snow need careful consideration.
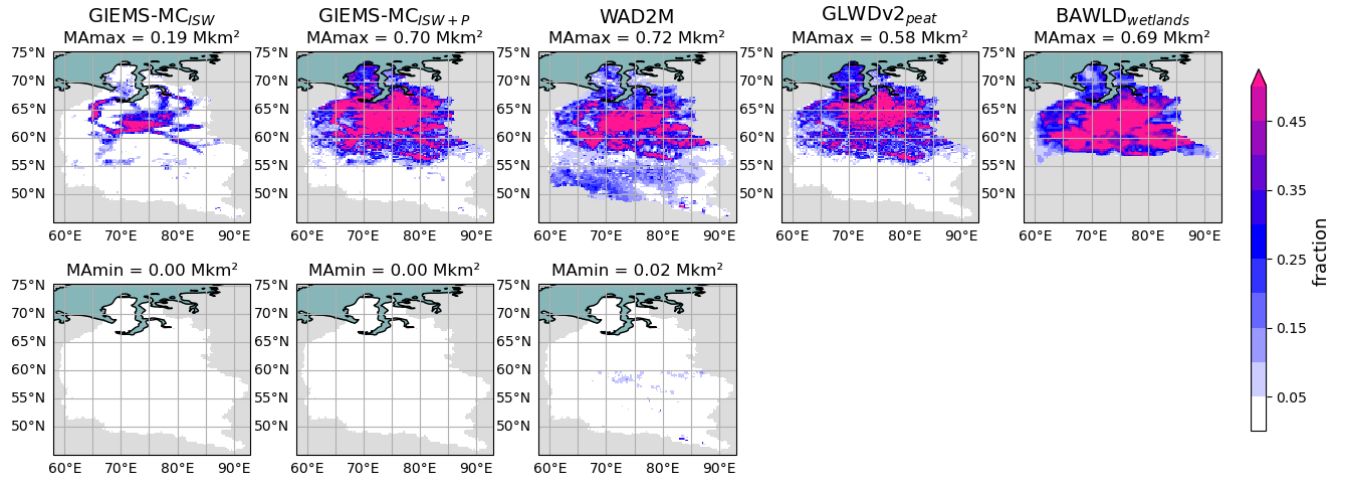
Figure 4. MAmax and MAmin maps of GIEMS-MC$_{ISW}$ (1992 to 2020), GIEMS-MC$_{ISW+P}$ (1992 to 2020), and WAD2M (2000 to 2020) over the Ob, as well as GLWDv2 peatland (static) and BAWLD wetland (static) maps. Low MAmin are due to the snow mask.
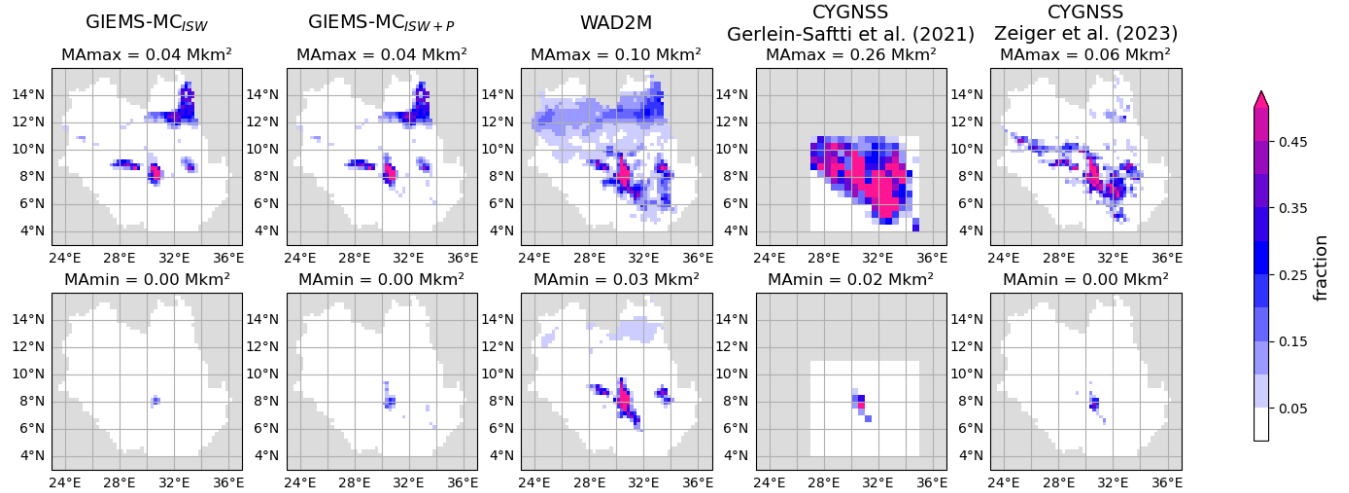
Figure 5. MAmax and MAmin maps over the Sudd region of GIEMS-MC$_{ISW}$, GIEMS-MC$_{ISW+P}$ (1992 to 2020), WAD2M (2000 to 2020) and CYGNSS-based estimates from Gerlein-Safdi et al. (2021) (2017-Jun to 2020-Apr) and Zeiger et al. (2023) (2018-Aug to 2020-Jul). The available periods differ between the products.
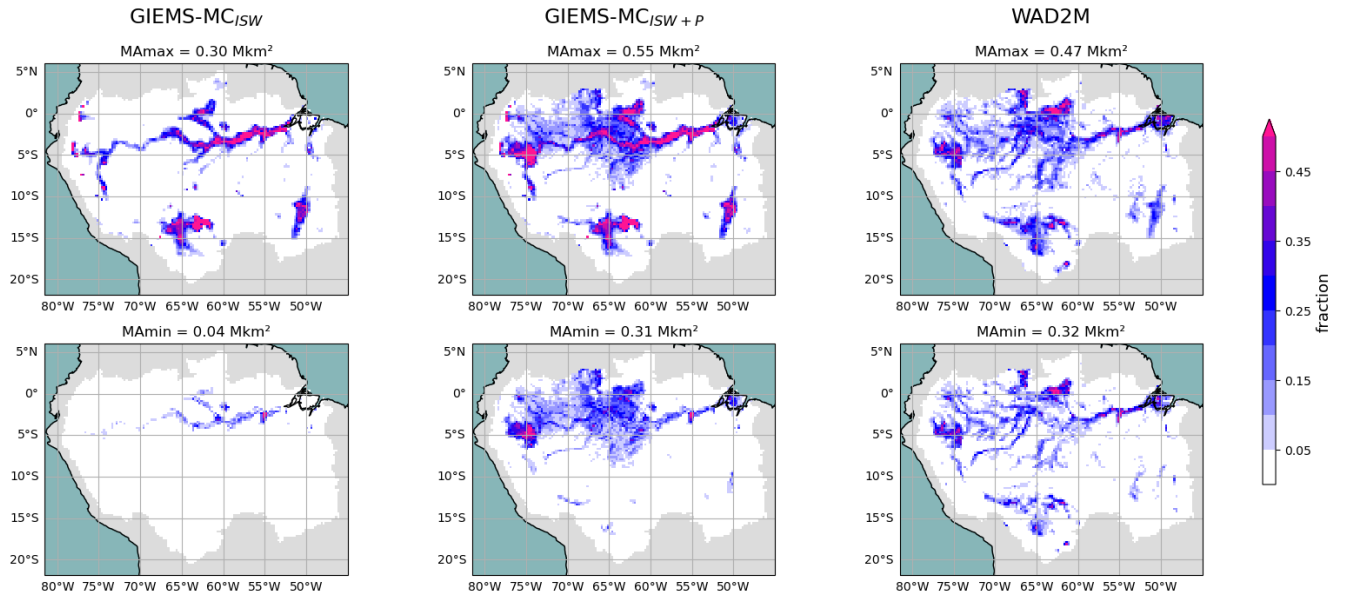
Figure 6. MAmax and MAmin maps of GIEMS-MC_{ISW} (1992 to 2020), GIEMS-MC_{ISW+P} (1992 to 2020), and WAD2M (2000 to 2020) over the Amazon basin.
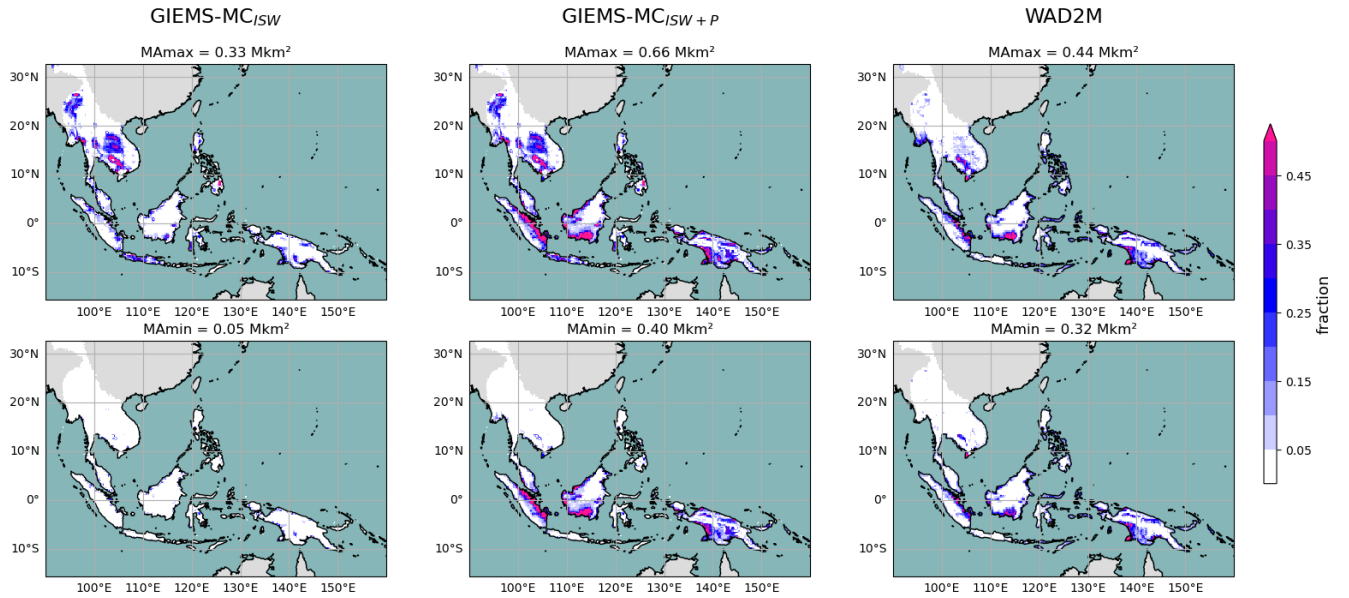
Figure 7. MAmax and MAmin maps of GIEMS-MC_{ISW} (1992 to 2020), GIEMS-MC_{ISW+P} (1992 to 2020), and WAD2M (2000 to 2020) over South-East Asia.

4.3 Temporal seasonal and inter-annual variations

The temporal dynamics of GIEMS-2 was extensively examined in Prigent et al. (2020) and evaluated in Bernard et al. (2024b), where it was compared with other hydrological observations, including MODIS-derived surface water extent (Frappart et al., 2018; Normandin et al., 2018, 2024), CYGNSS-derived (Zeiger et al., 2023) surface water extent, and river discharge. The evaluation showed that GIEMS-2 reliably captures temporal variations, including seasonality and inter-annual variabilities, even in regions with dense vegetation cover (Fig. 8 and Fig. 9).
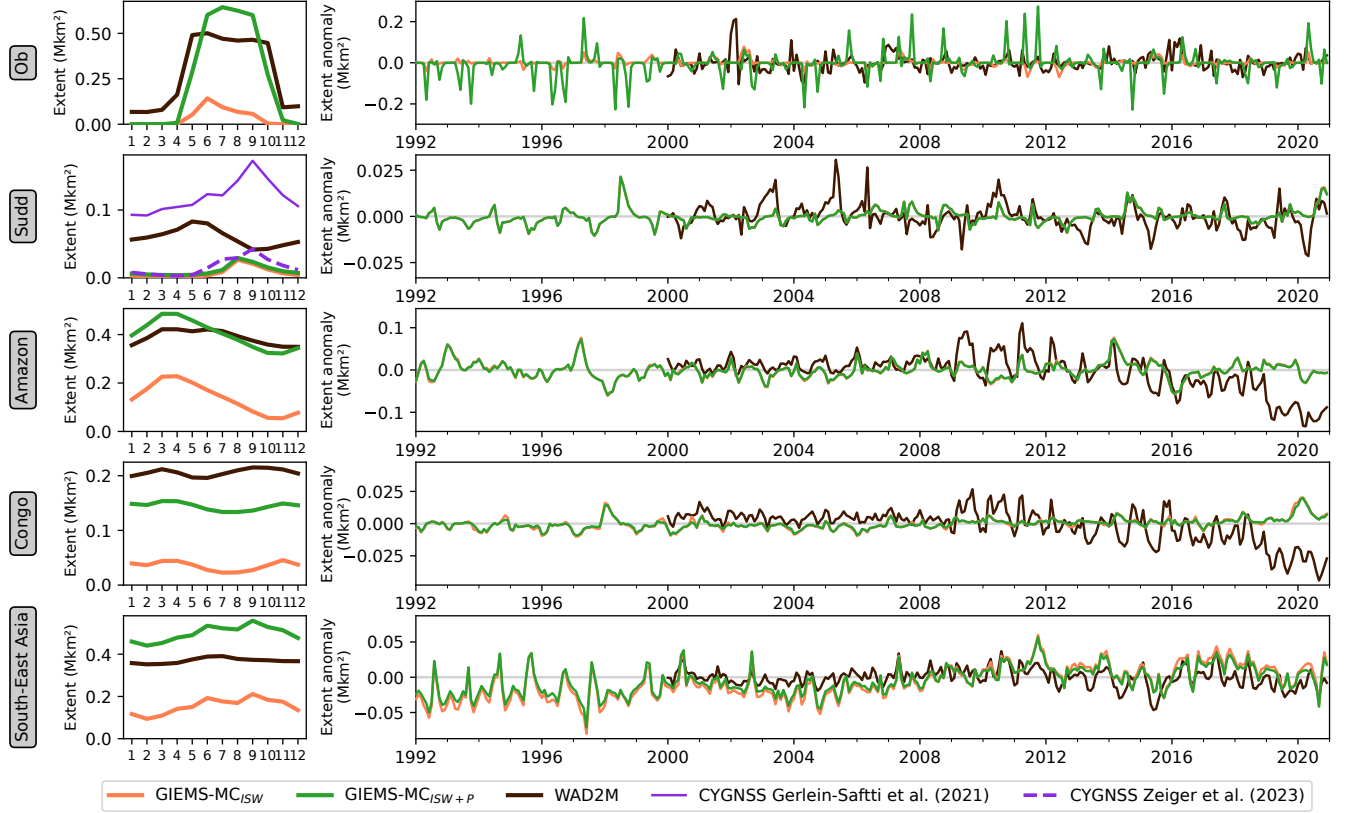
Figure 8. Left: Monthly mean seasonal cycle of GIEMS-MC$_{ISW}$, GIEMS-MC$_{ISW+P}$, and WAD2M over different regions. Right: Deseasonalized monthly anomalies of the same three variables. To derive the deseasonalized monthly anomalies, the average monthly seasonal cycle was subtracted from the long term monthly time series. For the Sudd basin seasonality comparison, estimations from Gerlein-Safdi et al. (2021) (2017-06 to 2020-04) and Zeiger et al. (2023) (2018-08 to 2020-07) are added.
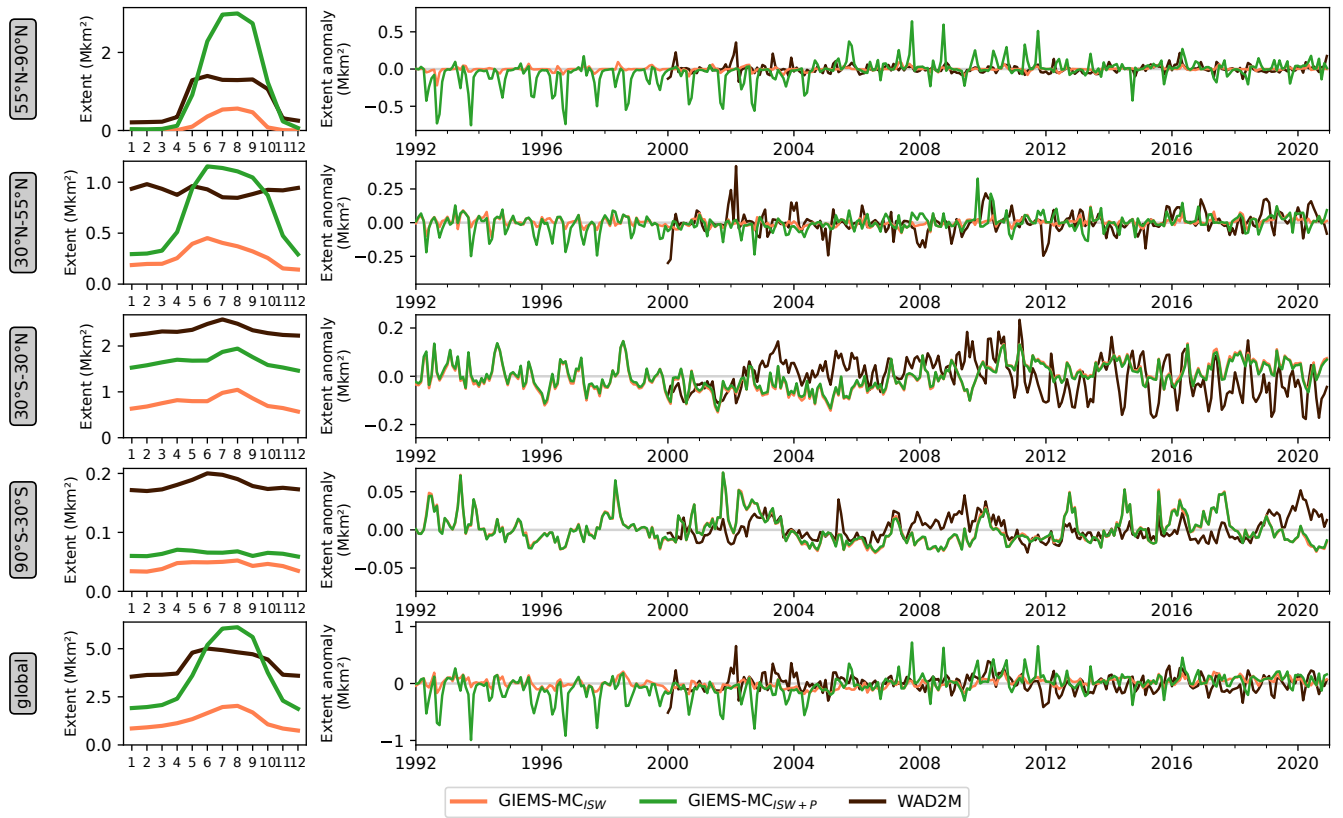
Figure 9. Left: Monthly mean seasonal cycle of GIEMS-MC$_{ISW}$, GIEMS-MC$_{ISW+P}$, and WAD2M over different latitudinal bands. Right: Deseasonalized monthly anomalies of the same three variables. To derive the deseasonalized monthly anomalies, the average monthly seasonal cycle was subtracted from the long term monthly time series.

4.3.1 Seasonal variations

350   The 2000-2020 mean seasonality of GIEMS-MC$_{ISW}$, GIEMS-MC$_{ISW+P}$, and WAD2M over the Ob, the Sudd, the Amazon, the Congo, and South-East Asia, are presented in Fig. 8 (left). The seasonal variations of the GIEMS-MC variables are driven by the dynamics of saturated and inundated wetlands (GIEMS-MC$_{ISW}$), with peatlands contributing to an offset effect between GIEMS-MC$_{ISW}$ and GIEMS-MC$_{ISW+P}$. In the Ob, the Amazon, the Congo, and South-East Asia, GIEMS-MC$_{ISW+P}$ exhibits comparable magnitudes than WAD2M. In the Sudd region, WAD2M shows distinct seasonality than GIEMS-MC and the two
355   CYGNSS derived products, probably due to the SWAMPS artifacts in desert regions mentioned above.

Across latitudinal bands, the global seasonality of GIEMS-MC$_{ISW}$ and GIEMS-MC$_{ISW+P}$ are mainly driven by the boreal and temperate northern regions, due to snow cover changes (Fig. 9, left). However, notable differences in terms of seasonal cycle between GIEMS-MC$_{ISW+P}$ and WAD2M exist over the mid to high latitudes. Indeed, larger peatland surfaces are included in GIEMS-MC than in WAD2M (higher amplitude) and the more widespread snow masking in GIEMS-MC in the temperate

360   zone leads to a stronger seasonal cycle compared to WAD2M. The seasonal cycles over the tropics and southern hemisphere are more similar between GIEMS-MC$_{ISW+P}$ and WAD2M, but surface extents are larger in WAD2M, predominantly due to desert and ocean contamination in SWAMPS, as discussed in Sect. 4.1.

4.3.2   Inter-annual variations & trends

    Figure 8 (right) shows the deseasonalized monthly anomalies of GIEMS-MC$_{ISW}$, GIEMS-MC$_{ISW+P}$, and WAD2M over differ-
365 ent regions, while Fig. 9 (right) corresponds to latitudinal bands. The reference seasonality period subtracted is the 2000-2020 seasonal average. As expected, GIEMS-MC$_{ISW}$ and GIEMS-MC$_{ISW+P}$ have the same anomalies for latitudes below 30°N because the temporal dynamics comes from the inundated and saturated wetlands, and not from the static peatland map. For northern temperate and boreal areas, the snow cover also imposes a seasonality on peatlands, which explains larger anomalies of GIEMS-MC$_{ISW+P}$ than in GIEMS-MC$_{ISW}$. For GIEMS-MC$_{ISW+P}$ over the boreal region (55°N-90°N), a positive trend is
370 detected over May and June (+10 10^3 km^2 yr^{-1}) and September and October (+24 10^3 km^2 yr^{-1}) months that can possibly be attributed to earlier snow melt and delayed snow cover arrival.

    No long-term trends were found at regional scales in GIEMS-MC$_{ISW}$, except for South-East Asia, where a small positive trend was found (+1.7 10^3 km^2 yr^{-1}, i.e. ~+50 10^3 km^2 for 30 yr). This is likely mostly due to the increasing trend in rice paddies, which is not taken into account because only the MIRCA2000 climatology is used, and new rice paddies over the
375 years are then aliased to wetlands over time (see Discussion Sect.5.2.2).

    An abrupt change in WAD2M inter-annual variability amplitude occur over the Amazon and Congo basins in 2009, attributed to a change in one of the satellite data used in SWAMPS, together with a decreasing trend also found in the SWAMPS data (Fig. 8). Due to these problems in SWAMPS, the inter-annual variability of WAD2M should be considered with caution, and makes time-series comparison with GIEMS-MC$_{ISW+P}$ difficult over these regions.

380 ## 5   Discussion

    The production of GIEMS-MC involves seven steps, each of which contributes to the transition from inundation time series to wetland map time series, but also to the uncertainties of the final product. It has been estimated that the GIEMS product possibly underestimates surface water areas by less than 10% (Prigent et al., 2007). This value can be used as an order of magnitude of the uncertainty in GIEMS-2, although methodological improvements have been made between GIEMS and GIEMS-2 (Prigent
385 et al., 2020). This is also likely a realistic approximation for the GIEMS-MC$_{ISW}$ error, as it uses mainly GIEMS-2 information. A quantification of the uncertainties of the GIEMS-MC variables would require a deeper knowledge of the measurement and detection uncertainties of all the products used, some of which are not calculated in the original source, which is beyond the scope of this study. However, it is possible to quantify the influence of each step in the GIEMS-MC procedure and to study the sensitivity of the results to the processing choices.

5.1 Quantification of the influence of each process step on the GIEMS-MC global extents

Table 4 shows the influence of the successive steps in terms of MAmax, MAmean and MAmin. The removal of open permanent water (Step 4.), as well as the subtraction of rice paddies (Step 5.), have a significant impact on the global extent, both resulting in a subtraction of -2.34 Mkm^2 on MAmax and -1.16 Mkm^2 on MAmean. Coastal cleaning also has a large influence on the reduction of the area: -2.60 Mkm^2 in MAmax and -1.60 Mkm^2 in MAmean, and especially on MAmin, which decreases from 1.17 Mkm^2 to 0.26 Mkm^2. In fact, the coastal region has an artificially high minimum value due to ocean contamination before this cleaning step. Finally, the addition of peatlands turns out to be an extremely significant step in terms of surface area for GIEMS-MC$_{ISW+P}$, with large increases observed in both MAmax (+3.94 Mkm^2) and MAmean (+2.27 Mkm^2) extents.

Step	Step description	MAmax	MAmean	MAmin
0	GIEMS-2 revised version	9.02	4.15	1.63
1 to 3	After masking oceans, snow and urban areas	8.83	4.03	1.58
4	After subtracting open permanent water	6.89	3.06	1.23
5	After subtracting rice paddies	6.30	2.77	1.12
6	After cleaning coasts (GIEMS-MC$_{ISW}$)	**3.80**	**1.23**	**0.25**
7	After adding peatlands (GIEMS-MC$_{ISW+P}$)	**7.75**	**3.50**	**1.31**

Table 4. Global MAmax, MAmean and MAmin in Mkm^2 after each step of GIEMS-MC production. It should be noted that snow and oceans were already set to zero fraction in GIEMS-2, and that the snow mask is applied to all wetlands, including peatlands, and is then responsible for the low MAmin values.

5.2 Sensitivity to the GIEMS-MC procedure

The three critical stages in the production of GIEMS-MC are further discussed in this section, along with the use of a snow mask.

5.2.1 Coastal processing

In the Methods Sect. 3.1.6, we chose to apply a cleaning procedure to coastal pixels located within 50 km of the coast. Figure 10.a shows the global mean seasonality of GIEMS-MC$_{ISW}$ and GIEMS-MC$_{ISW+P}$ when considering coastal bands ranging between 0 and 100 km from the coast to be processed using GLWDv2 information, following the methodology in Sect. 3. After removing the pixels with more than 10% ocean, the cleaning of the coastal band up to 30 km from the coast reduces GIEMS-MC$_{ISW}$ MAmax by 0.7 Mkm^2. Cleaning also the 30-50 km band reduces it further by 0.5 Mkm^2, while the 50-70 km (-0.12 Mkm^2) and 70-100 km (-0.08 Mkm^2) bands have smaller effects. The cleaning over 50 km is consistent with our technical understanding of the contamination.
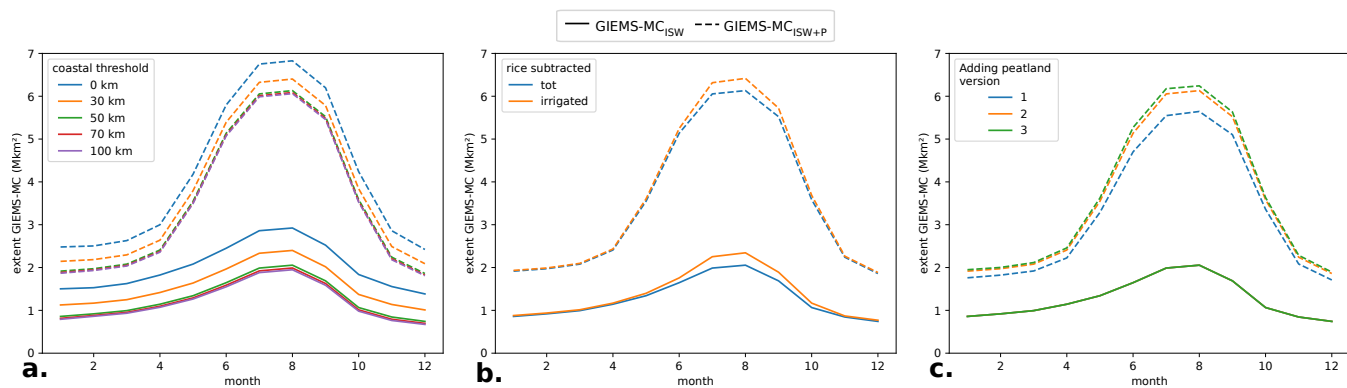
Figure 10. Sensitivity of GIEMS-MC averaged seasonality to the different steps of the production procedure : **a.** the coastal threshold for coastal cleaning, **b.** the rice procedure, and **c.** the way peatlands are added. Solid lines represent the extent of GIEMS-MC$_{ISW}$, while dashed lines represent GIEMS-MC$_{ISW+P}$. Colors show the different GIEMS-MC treatments.

5.2.2 Rice subtraction

410 An issue concerning rice in GIEMS-MC production stems from the classification used in the MIRCA2000 dataset, which separates rice paddies into irrigated and rainfed types. Irrigated paddies are typically fully inundated at least part of the year. Rainfed paddies have variable levels of submergence, with approximately 80% inundated and 20% remaining upland paddies (Maclean et al., 2013). Under these conditions, the upland rice (9% of total rice paddies area ; Maclean et al. (2013)) should not be subtracted from GIEMS-2 in the GIEMS-MC processing steps, if we could distinguish upland rice from the rest of

415 the rainfed paddies. To explore this, we attempted a classification based on topographic information to separate inundated from non-inundated within the rainfed rice category. The resulting maps, shown in Supplementary Table S3, lead to surface extent inconsistent with FAO statistics per country (FAO, 2002). In the absence of any reliable distinction possibility, the total rice paddies were subtracted, acknowledging that the subtracted area might be overestimated by about 9%. Note that this light overestimation of subtracted rice paddies might be counterbalanced by the fact that MIRCA2000 areas estimates are

420 underestimated when compared to FAOSTAT (Fig. 11).

In WAD2M production, the MIRCA2000 is also used to differentiate rice paddies from wetlands, but only irrigated paddy class is subtracted (Zhang et al., 2021b). To evaluate the impact of rice handling in GIEMS-MC, Fig. 10.b shows global seasonality of GIEMS-MC$_{ISW}$ and GIEMS-MC$_{ISW+P}$ if only irrigated rice paddies are subtracted, or if both irrigated and rainfed are subtracted. The difference occurs mainly between June and October, in the Northern Hemisphere summer, corresponding

425 to a difference of 0.25 Mkm^2 in terms of MAmax (6% of GIEMS-MC$_{ISW}$ and 3% GIEMS-MC$_{ISW+P}$ MAmax). While this has a moderate influence on global extent, this difference can be important in rice cultivating countries, e.g., a difference of 30% in GIEMS-MC$_{ISW}$ MAmax over India depending on the type of subtraction used. For GIEMS-MC$_{ISW+P}$, as the total surfaces are higher, the influence of rice paddy subtraction is proportionally less important.

Finally, subtracting the MIRCA2000 climatology in the GIEMS-MC processing and not taking into account the inter-annual

430 variation of rice paddies and their inter-annual changes in inundation over the period 1992-2020 can lead to misclassifica-

tion of rice paddies as wetlands. First, rainfed rice paddies in particular show significant inter-annual changes in inundation. Furthermore, the surface covered by rice paddies also changes over the years. The MIRCA2000 product is compared in Fig. 11 with the estimates from the Food and Agriculture Organization (FAO) of the United Nations estimates FAOSTAT (https://www.fao.org/faostat/en/#data/QCL, access 30/06/2023). FAOSTAT is widely used for global estimates of methane
435 emissions from rice paddies, notably in the Emissions Database for Global Atmospheric Research (EDGAR ; Janssens-Maenhout et al. (2019)). The cropland area of rice paddies is increasing in South-East Asia, with FAOSTAT estimating +60 10^3 km^2 between 1992 and 2020 in this region, which corresponds to the increasing trend of ~+50 10^3 km^2 in GIEMS-MC$_{\text{ISW}}$ over this period (Sect. 4.3.2).

MIRCA2000 (MAmax of 1.25 Mkm^2) presents smaller rice paddies extent than FAOSTAT (1.47 Mkm^2 in 1992 to 1.64 Mkm^2
440 in 2020). In GLWDv2, the map from Salmon et al. (2015) is used as primary information but undergoes numerous corrections related to artifacts in the product, including double-checking information using the RiceAtlas (Laborte et al., 2017). This lead to a static map of rice paddies of 1.2 Mkm^2, close to MIRCA2000 MAmax estimates. Then, various inventories of anthropogenic methane emissions that are accounting for rice methane emissions are not using the same maps for rice paddies, which can lead to mismatches across the estimates (surfaces double counting or miscounting). Efforts to use similar compatible rice maps
445 between the two research communities would greatly improve the consistency of wetland time series, and then the methane emission estimates. A dynamic map that accurately reflects the temporal variation of inundated rice paddies would better meet the needs of remote sensing wetland mapping. This approach would address the limitations of existing classifications, such as MIRCA's irrigated/rainfed or FAO's yearly irrigated/rainfed/upland categories, which do not adequately address the specific needs of the community.
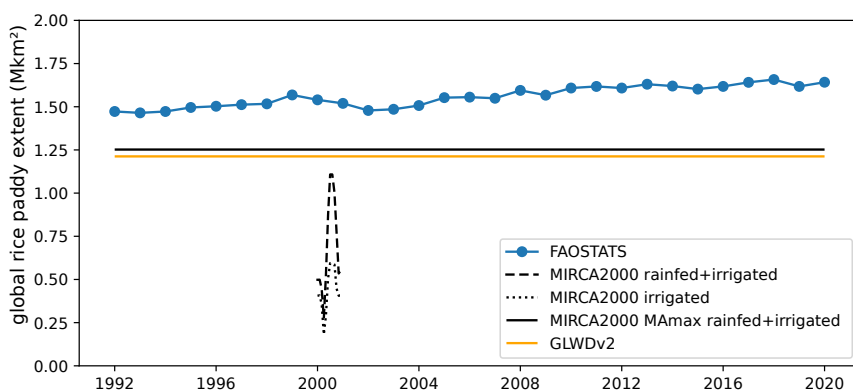
Figure 11. Rice paddy surface extent estimations from MIRCA2000 (Portmann et al., 2010), FAOSTAT (https://www.fao.org/faostat/en/#data/QCL), and GLWDv2 (Lehner et al., 2024a). MIRCA2000 MAmax is higher than the maximum of the MIRCA2000 seasonality plot because not all pixels have their maximum in the same month.

5.2.3 Peatland integration

Peatlands contribute to more than a half of areas in GIEMS-MC$_{ISW+P}$ (Table 4), and depends highly on the GLWDv2 peatland map used here.

Most of the peatlands are not saturated or inundated areas, although some can have their water table above the peat surface intermittently (Lourenco et al., 2023). A large part of peatlands are then not detected by GIEMS-2. Three ways of integrating GLWDv2 peatlands were tested to assess how sensitive the peatlands integration method is. For each pixel i, we did the following:

1. Set GLWDv2$_{peat}$ fraction as the minimum of GIEMS-MC$_{ISW+P}$, minimizing GIEMS-MC$_{ISW+P}$ areas:
   if GIEMS-MC$_{ISW i}$<GLWDv2$_{peat i}$, then GIEMS-MC$_{ISW+P i}$=GLWDv2$_{peat i}$.

2. Attempt to add only the peatlands not detected by GIEMS-2 as described in Methods Sect. 3.1.7:
   GIEMS-MC$_{ISW+P i}$=GIEMS-MC$_{ISW i}$ + pos[GLWDv2$_{peat i}$ - pos(GIEMS-MC$_{ISW i}$ - GLWDv2$_{ISW+P i}$)]

3. Add all GLWDv2 peatland, maximizing GIEMS-MC$_{ISW+P}$ areas:
   GIEMS-MC$_{ISW+P i}$=GIEMS-MC$_{ISW i}$+GLWDv2$_{peat i}$.

The effect of these three peatland integration approaches on GIEMS-MC$_{ISW+P}$ extent are represented in Fig. 10.c. A difference of 0.85 Mkm^2 (11%) is found for GIEMS-MC$_{ISW+P}$ MAmax between the two extreme approaches 1 and 3. Approach 1 likely underestimates peatland integration, as some pixels can contain both inundated or saturated wetlands and peatlands. Approach 3 likely overestimates peatland integration, as some peatlands (inundated and saturated) should be detected in GIEMS-2. The method 2 appears as a sensible consensus, but this approach also likely overestimates peatland surfaces, as GLWDv2 wetland categories, used to discriminate detected and non-detected peatlands by GIEMS-2 (see Sect. 3.1.7), is a long term maximum.

Non-inundated peatlands account for a significant proportion of the GIEMS-MC$_{ISW+P}$ in terms of maximum area (50.2% of the MAmax, see Table 2). The peatland map used in this study to derive GIEMS-MC$_{ISW+P}$ comes from GLWDv2, and is a composite product based on four different estimates (see section 3.1.7 or Lehner et al. (2024a)). It should be emphasized that although this product is based on the best current knowledge, there is still limited consensus in the literature on the extent of peatlands. Mapping of peatlands remains challenging, as it is primarily a soil characteristic related to organic carbon content that cannot be directly detected by satellite data. Consequently, mapping efforts rely on approaches based on observations (in situ data and / or remote sensing proxies for, e.g., vegetation or hydrological data) to map their extent using models or machine learning. This task is particularly difficult in tropical regions, where in situ data are sparse and where dense cloud and vegetation covers limit remote sensing observations, this results in fewer regional maps over the Tropics with frequent revisions towards higher estimates of tropical peatland areas (Dargie et al., 2017; Hastie et al., 2024).

5.2.4 Snow-covered pixel masking

Due to the influence of snow on passive microwave observations, snow-covered pixels are masked in the estimation of GIEMS-2 and GIEMS-MC inundation fractions (see 3.1.2). This masking prevents models from accounting for methane emissions from snow-covered areas. However, cold-season methane fluxes in arctic peatlands and tundra have been shown to contribute between 25% and 50% of the annual local fluxes (Bao et al., 2021; Ito et al., 2023; Mastepanov et al., 2008; Rößger et al., 2022; Zona et al., 2016). Therefore, the sensitivity of microwave remote sensing to snow is a limitation in boreal regions. Nevertheless, the boreal zones are estimated to contribute only about 5% of annual global wetland and inland freshwater emissions using a top-down approach, and about 10% using a bottom-up approach (Saunois et al., 2024), with only up to half of these boreal emissions potentially occurring during the cold season. Consequently, the exclusion of snow-covered areas is likely to add only a few percents of uncertainty to global methane emissions from wetlands and inland waters.

For consistency with the snow mask used in GIEMS-2 production, we have used the same mask here in the GIEMS-MC generation. This mask is derived from the ERA5 product, which might overestimate the extent of snow cover but still captures interannual changes well (Kouki et al., 2023). The snow mask in GIEMS-MC is only a filter for pixels potentially contaminated by the presence of snow. The potential overestimation of snow cover extent should have limited implications for methane emissions, as methane emissions in these regions during the snow season should be a small fraction of global emissions, as discussed above.

6 Perspectives

Several key areas for future improvement of the GIEMS-MC production process were identified. First, taking into account the inter-annual variations of rice paddies would help improve the accuracy and in particular the long-term trend of GIEMS-MC. Ideally, these estimates should be consistent with those used in anthropogenic greenhouse gas emission inventories such as FAOSTAT. Secondly, a better distinction between inundated and dry peatlands would allow a more accurate integration of peatlands into GIEMS-MC$_{ISW+P}$. New satellite data, such as the 2022-launched Surface Water and Ocean Topography (SWOT) with its Ka-band Radar Interferometer, hold promise for the monitoring of continental surface water area and height at high spatial resolution and temporal sampling (Neeck et al., 2012; Pedinotti et al., 2014; Biancamaria et al., 2016; Prigent et al., 2016; Peral and Esteban-Fernandez, 2018). In particular, either high resolution SWOT data or water table depth from a hydrological model combined with the 500 m GLWDv2 data could help to better distinguish the inundated from the non-inundated peatlands to improve the integration of non-inundated peatlands in GIEMS-MC$_{ISW+P}$. In addition, the upcoming NASA-ISRO Synthetic Aperture Radar (NISAR), scheduled for launch in 2025, will provide high-resolution (below 7 m) observations in L and S bands (Chuang et al., 2016; Adeli et al., 2021). These frequencies are particularly advantageous for mapping of sub-canopy inundation in forested wetlands, as they penetrate vegetation more effectively than the Ka band used for SWOT.

GIEMS-MC dynamics is derived from GIEMS-2, which provides valuable insights into global water surface dynamics with seamless time series of surface water extent. The continuity of GIEMS-2 production holds the potential to extend the temporal

coverage of the GIEMS-MC maps. However, no new SSMIS instrument is planned to be launched when the current instruments (F15 to F18) are decommissioned. Adaptations to the GIEMS-2 process, such as the incorporation of Advanced Microwave Scanning Radiometer (AMSR) data, will be required to extend the observation period despite critical changes in satellite overpassing local time and spatial resolution. Other passive microwave future missions are expected to cover all or part of the SSMIS microwave frequency range, such as the MicroWave Imager (MetOp-SG, D'Addio et al. (2014)) or the Copernicus Imaging Microwave Radiometer (CIMR, Vanin et al. (2020)), offering alternative data sources for GIEMS-MC production but also requiring adjustment to the methodology. In addition, plans to increase the temporal resolution of GIEMS-2 to a 10-day data record could provide a more detailed understanding of wetland dynamics over time.

7 Conclusion

Despite significant advances in methane measurement and modelling, accurate mapping of wetland extent remains a key challenge. In this context, we introduce GIEMS-MethaneCentric (GIEMS-MC). It is a new product that improves the temporal variability of the wetland extent by accurately capturing seasonal and interannual dynamics without discontinuities, while also enhancing spatial patterns.

GIEMS-2 product was combined with other information to produce GIEMS-MC, a dataset containing spatially and dynamically consistent maps of different methane-emitting aquatic ecosystems. In particular, GLWDv2 dataset enables the separation of open water surfaces (lakes, rivers, reservoirs) in GIEMS-2, as well as the addition of peatlands not detected by microwaves satellite observations used in GIEMS-2 production. Rice paddies are identified using the MIRCA2000 product. Updated coastal zone filtering improves on the previous complete masking in the distributed version of GIEMS-2.

GIEMS-MC provides two harmonized times series maps at 0.25°x0.25° and monthly time step of wetland surfaces from 1992 to 2020: one representing inundated and saturated wetlands, and the other covering all wetlands, including peatlands. In addition, GIEMS-MC provides consistent maps of rice paddies and categories of open permanent water. Information on the dominant vegetation and wetland type for each pixel is also provided, as these factors help improve the understanding and accurate modeling of methane emissions from wetlands.

This comprehensive database will hopefully set a new standard for harmonizing and consistently mapping methane emission from the different aquatic ecosystems.

Data availability. GIEMS-MC dataset in NetCDF format and its documentation are available at https://doi.org/10.5281/zenodo.13919645 (Bernard et al., 2024a). GIEMS-2 production is available upon request to catherine.prigent@obspm.fr. GLWDv2 is available at https://www.hydrosheds.org/products/glwd, MIRCA2000 at https://doi.org/10.5281/zenodo.7422506, ESA CCI at https://doi.org/10.5194/essd-15-1465-2023, WAD2M at https://doi.org/10.5281/zenodo.3998454, BAWLD at https://doi.org/10.18739/A2C824F9X and CYGNNS products at https://doi.org/10.6096/3003 and https://doi.org/10.5281/zenodo.5621107.

Author contributions. J.B., C.P., C.J., M.S. and E.F-C. conceived the main ideas of this study. C.J. and C.P. developped and produced the GIEMS-2 data. B.L. provided GLWDv2 product. J.B., C.J., and C.P. built the database and performed the numerical analyses. J.B. drafted the manuscript with input from C.P., M.S, and E.F-C. All authors provided critical feedbacks and expertise on the manuscript.

Competing interests. The authors declare no competing interests.

Acknowledgements. Juliette Bernard is funded by a PhD grant from the Institut National des Sciences de l'Univers (INSU) of the Centre National de la Recherche Scientifique (CNRS). Partial funding has been provided by the ESA CCI RECAPP2 project (4000123002/18/INB), and a preliminary version of this database has been developed under that contract. The Agence National de la Recherche also provided support through the project Advanced Methane Budget through Multi-constraints and Multi-data streams Modelling (AMB-M3 - ANR-21-CE01-0030). The authors would like to thank Pierre Zeiger and Frédéric Frappart for the discussions on their CYGNSS-derived wetland extent dataset. The authors thank the three anonymous reviewers for their comments and suggestions.

References

Adeli, S., Salehi, B., Mahdianpari, M., Quackenbush, L. J., and Chapman, B.: Moving Toward L-Band NASA-ISRO SAR Mission (NISAR) Dense Time Series: Multipolarization Object-Based Classification of Wetlands Using Two Machine Learning Algorithms, Earth and Space Science, 8, e2021EA001 742, https://doi.org/10.1029/2021EA001742, 2021.

Aires, F., Miolane, L., Prigent, C., Pham, B., Fluet-Chouinard, E., Lehner, B., and Papa, F.: A Global Dynamic Long-Term Inundation Extent Dataset at High Spatial Resolution Derived through Downscaling of Satellite Observations, Journal of Hydrometeorology, 18, 1305–1325, https://doi.org/10.1175/JHM-D-16-0155.1, 2017.

Allen, G. H. and Pavelsky, T. M.: Global Extent of Rivers and Streams, Science, 361, 585–588, https://doi.org/10.1126/science.aat0636, 2018.

Bao, T., Xu, X., Jia, G., Billesbach, D. P., and Sullivan, R. C.: Much Stronger Tundra Methane Emissions during Autumn Freeze than Spring Thaw, Global Change Biology, 27, 376–387, https://doi.org/10.1111/gcb.15421, 2021.

Bartholomé, E. and Belward, A. S.: GLC2000: A New Approach to Global Land Cover Mapping from Earth Observation Data, International Journal of Remote Sensing, 26, 1959–1977, https://doi.org/10.1080/01431160412331291297, 2005.

Bernard, J., Prigent, C., Jimenez, C., Fluet-Chouinard, E., Lehner, B., Salmon, E., Ciais, P., Zhen, Z., Peng, S., and Saunois, M.: GIEMS-MethaneCentric, https://doi.org/10.5281/zenodo.13919645, 2024a.

Bernard, J., Prigent, C., Jimenez, C., Frappart, F., Normandin, C., Zeiger, P., Xi, Y., and Peng, S.: Assessing the Time Variability of GIEMS-2 Satellite-Derived Surface Water Extent over 30 Years, Frontiers in Remote Sensing, 5, 1399 234, https://doi.org/10.3389/frsen.2024.1399234, 2024b.

Biancamaria, S., Lettenmaier, D. P., and Pavelsky, T. M.: The SWOT Mission and Its Capabilities for Land Hydrology, Surveys in Geophysics, 37, 307–337, https://doi.org/10.1007/s10712-015-9346-y, 2016.

Bousquet, P., Ciais, P., Miller, J. B., Dlugokencky, E. J., Hauglustaine, D. A., Prigent, C., Van Der Werf, G. R., Peylin, P., Brunke, E.-G., Carouge, C., Langenfelds, R. L., Lathière, J., Papa, F., Ramonet, M., Schmidt, M., Steele, L. P., Tyler, S. C., and White, J.: Contribution of Anthropogenic and Natural Sources to Atmospheric Methane Variability, Nature, 443, 439–443, https://doi.org/10.1038/nature05132, 2006.

Bridgham, S. D., Cadillo-Quiroz, H., Keller, J. K., and Zhuang, Q.: Methane Emissions from Wetlands: Biogeochemical, Microbial, and Modeling Perspectives from Local to Global Scales, Global Change Biology, 19, 1325–1346, https://doi.org/10.1111/gcb.12131, 2013.

Canadell, J., Monteiro, P., Costa, M., Cotrim da Cunha, L., Cox, P., Eliseev, A., Henson, S., Ishii, M., Jaccard, S., Koven, C., Lohila, A., Patra, P., Piao, S., Rogelj, J., Syampungani, S., Zaehle, S., and Zickfeld, K.: Global Carbon and other Biogeochemical Cycles and Feedbacks, in: Climate Change 2021: The Physical Science Basis. Contribution of Working Group I to the Sixth Assessment Report of the Intergovernmental Panel on Climate Change, edited by Masson-Delmotte, V., Zhai, P., Pirani, A., Connors, S. L., Péan, C., Berger, S., Caud, N., Chen, Y., Goldfarb, L., Gomis, M. I., Huang, M., Leitzell, K., Lonnoy, E., Matthews, J. B. R., Maycock, T. K., Waterfield, T., Yelekçi, O., Yu, R., and Zhou, B., book section 5, Cambridge University Press, Cambridge, UK and New York, NY, USA, https://doi.org/10.1017/9781009157896.007, 2021.

Carroll, M., Townshend, J., DiMiceli, C., Noojipady, P., and Sohlberg, R.: A New Global Raster Water Mask at 250 m Resolution, International Journal of Digital Earth, 2, 291–308, https://doi.org/10.1080/17538940902951401, 2009.

Chapman, B., McDonald, K., Shimada, M., Rosenqvist, A., Schroeder, R., and Hess, L.: Mapping Regional Inundation with Spaceborne L-Band SAR, Remote Sensing, 7, 5440–5470, https://doi.org/10.3390/rs70505440, 2015.

590 Chuang, C.-L., Shaffer, S., Niamsuwan, N., Li, S., Liao, E., Lim, C., Duong, V., Volain, B., Vines, K., Yang, M.-W., and Wheeler, K.: NISAR L-band Digital Electronics Subsystem: A Multichannel System with Distributed Processors for Digital Beam Forming and Mode Dependent Filtering, in: 2016 IEEE Radar Conference (RadarConf), pp. 1–5, IEEE, Philadelphia, PA, USA, ISBN 978-1-5090-0863-6, https://doi.org/10.1109/RADAR.2016.7485225, 2016.

D'Addio, S., Kangas, V., Klein, U., Loiselet, M., and Mason, G.: The Microwave Radiometers On-Board MetOp Second Generation
595 Satellites, in: 2014 IEEE Metrology for Aerospace (MetroAeroSpace), pp. 599–604, IEEE, Benevento, Italy, ISBN 978-1-4799-2069-3, https://doi.org/10.1109/MetroAeroSpace.2014.6865995, 2014.

Dargie, G. C., Lewis, S. L., Lawson, I. T., Mitchard, E. T. A., Page, S. E., Bocko, Y. E., and Ifo, S. A.: Age, Extent and Carbon Storage of the Central Congo Basin Peatland Complex, Nature, 542, 86–90, https://doi.org/10.1038/nature21048, 2017.

Di Gregorio, A. and Jansen, L. J.: Land Cover Classification System (LCCS): Classification Concepts and User Manual, https://www.fao.
600 org/3/x0596e/x0596e00.htm, 2005.

ESA: Land Cover CCI. Product User Guide Version 2.0, Tech. rep., ESA, 2017.

FAO: FAO Rice Information, Volume 3, FAO, 2002.

Feng, M., Sexton, J. O., Channan, S., and Townshend, J. R.: A Global, High-Resolution (30-m) Inland Water Body Dataset for 2000: First Results of a Topographic–Spectral Classification Algorithm, International Journal of Digital Earth, 9, 113–133,
605 https://doi.org/10.1080/17538947.2015.1026420, 2016.

Fennig, K., Schröder, M., Andersson, A., and Hollmann, R.: A Fundamental Climate Data Record of SMMR, SSM/I, and SSMIS Brightness Temperatures, Earth System Science Data, 12, 647–681, https://doi.org/10.5194/essd-12-647-2020, 2020.

Feron, S., Malhotra, A., Bansal, S., Fluet-Chouinard, E., McNicol, G., Knox, S. H., Delwiche, K. B., Cordero, R. R., Ouyang, Z., Zhang, Z., Poulter, B., and Jackson, R. B.: Recent Increases in Annual, Seasonal, and Extreme Methane Fluxes Driven by Changes in Climate and
610 Vegetation in Boreal and Temperate Wetland Ecosystems, Global Change Biology, 30, e17 131, https://doi.org/10.1111/gcb.17131, 2024.

Fluet-Chouinard, E., Lehner, B., Rebelo, L.-M., Papa, F., and Hamilton, S. K.: Development of a Global Inundation Map at High Spatial Resolution from Topographic Downscaling of Coarse-Scale Remote Sensing Data, Remote Sensing of Environment, 158, 348–361, https://doi.org/10.1016/j.rse.2014.10.015, 2015.

Foster, J. L., Hall, D. K., Chang, A. T. C., and Rango, A.: An Overview of Passive Microwave Snow Research and Results, Reviews of
615 Geophysics, 22, 195–208, https://doi.org/10.1029/RG022i002p00195, 1984.

Frappart, F., Biancamaria, S., Normandin, C., Blarel, F., Bourrel, L., Aumont, M., Azemar, P., Vu, P.-L., Le Toan, T., Lubac, B., and Darrozes, J.: Influence of Recent Climatic Events on the Surface Water Storage of the Tonle Sap Lake, Science of The Total Environment, 636, 1520–1533, https://doi.org/10.1016/j.scitotenv.2018.04.326, 2018.

Friedl, M., McIver, D., Hodges, J., Zhang, X., Muchoney, D., Strahler, A., Woodcock, C., Gopal, S., Schneider, A., Cooper, A., Baccini, A.,
620 Gao, F., and Schaaf, C.: Global Land Cover Mapping from MODIS: Algorithms and Early Results, Remote Sensing of Environment, 83, 287–302, https://doi.org/10.1016/S0034-4257(02)00078-0, 2002.

Ge, M., Korrensalo, A., Laiho, R., Kohl, L., Lohila, A., Pihlatie, M., Li, X., Laine, A. M., Anttila, J., Putkinen, A., Wang, W., and Koskinen, M.: Plant-Mediated CH4 Exchange in Wetlands: A Review of Mechanisms and Measurement Methods with Implications for Modelling, Science of The Total Environment, 914, 169 662, https://doi.org/10.1016/j.scitotenv.2023.169662, 2024.

625 Gerlein-Safdi, C., Bloom, A. A., Plant, G., Kort, E. A., and Ruf, C. S.: Improving Representation of Tropical Wetland Methane Emissions With CYGNSS Inundation Maps, Global Biogeochemical Cycles, 35, https://doi.org/10.1029/2020GB006890, 2021.

Girkin, N. T., Siegenthaler, A., Lopez, O., Stott, A., Ostle, N., Gauci, V., and Sjögersten, S.: Plant Root Carbon Inputs Drive Methane Production in Tropical Peatlands, Scientific Reports, 15, 3244, https://doi.org/10.1038/s41598-025-87467-w, 2025.

Gumbricht, T., Roman-Cuesta, R. M., Verchot, L., Herold, M., Wittmann, F., Householder, E., Herold, N., and Murdiyarso, D.: An Expert System Model for Mapping Tropical Wetlands and Peatlands Reveals South America as the Largest Contributor, Global Change Biology, 23, 3581–3599, https://doi.org/10.1111/gcb.13689, 2017.

Hastie, A., Householder, J. E., Honorio Coronado, E. N., Hidalgo Pizango, C. G., Herrera, R., Lähteenoja, O., De Jong, J., Winton, R. S., Aymard Corredor, G. A., Reyna, J., Montoya, E., Paukku, S., Mitchard, E. T. A., Åkesson, C. M., Baker, T. R., Cole, L. E. S., Córdova Oroche, C. J., Dávila, N., Águila, J. D., Draper, F. C., Fluet-Chouinard, E., Grández, J., Janovec, J. P., Reyna, D., W Tobler, M., Del Castillo Torres, D., Roucoux, K. H., Wheeler, C. E., Fernandez Piedade, M. T., Schöngart, J., Wittmann, F., Van Der Zon, M., and Lawson, I. T.: A New Data-Driven Map Predicts Substantial Undocumented Peatland Areas in Amazonia, Environmental Research Letters, 19, 094 019, https://doi.org/10.1088/1748-9326/ad677b, 2024.

Hengl, T., Mendes de Jesus, J., Heuvelink, G. B. M., Ruiperez Gonzalez, M., Kilibarda, M., Blagotić, A., Shangguan, W., Wright, M. N., Geng, X., Bauer-Marschallinger, B., Guevara, M. A., Vargas, R., MacMillan, R. A., Batjes, N. H., Leenaars, J. G. B., Ribeiro, E., Wheeler, I., Mantel, S., and Kempen, B.: SoilGrids250m: Global Gridded Soil Information Based on Machine Learning, PLOS ONE, 12, e0169 748, https://doi.org/10.1371/journal.pone.0169748, 2017.

Hersbach, H., Bell, B., Berrisford, P., Hirahara, S., Horányi, A., Muñoz-Sabater, J., Nicolas, J., Peubey, C., Radu, R., Schepers, D., Simmons, A., Soci, C., Abdalla, S., Abellan, X., Balsamo, G., Bechtold, P., Biavati, G., Bidlot, J., Bonavita, M., De Chiara, G., Dahlgren, P., Dee, D., Diamantakis, M., Dragani, R., Flemming, J., Forbes, R., Fuentes, M., Geer, A., Haimberger, L., Healy, S., Hogan, R. J., Hólm, E., Janisková, M., Keeley, S., Laloyaux, P., Lopez, P., Lupu, C., Radnoti, G., De Rosnay, P., Rozum, I., Vamborg, F., Villaume, S., and Thépaut, J.-N.: The ERA5 Global Reanalysis, Quarterly Journal of the Royal Meteorological Society, 146, 1999–2049, https://doi.org/10.1002/qj.3803, 2020.

Hu, S., Niu, Z., and Chen, Y.: Global Wetland Datasets: A Review, Wetlands, 37, 807–817, https://doi.org/10.1007/s13157-017-0927-z, 2017.

Hugelius, G., Tarnocai, C., Broll, G., Canadell, J. G., Kuhry, P., and Swanson, D. K.: The Northern Circumpolar Soil Carbon Database: Spatially Distributed Datasets of Soil Coverage and Soil Carbon Storage in the Northern Permafrost Regions, 2013.

Ito, A., Li, T., Qin, Z., Melton, J. R., Tian, H., Kleinen, T., Zhang, W., Zhang, Z., Joos, F., Ciais, P., Hopcroft, P. O., Beerling, D. J., Liu, X., Zhuang, Q., Zhu, Q., Peng, C., Chang, K.-Y., Fluet-Chouinard, E., McNicol, G., Patra, P., Poulter, B., Sitch, S., Riley, W., and Zhu, Q.: Cold-Season Methane Fluxes Simulated by GCP-CH$_4$ Models, Geophysical Research Letters, 50, e2023GL103 037, https://doi.org/10.1029/2023GL103037, 2023.

Janssens-Maenhout, G., Crippa, M., Guizzardi, D., Muntean, M., Schaaf, E., Dentener, F., Bergamaschi, P., Pagliari, V., Olivier, J. G. J., Peters, J. A. H. W., Van Aardenne, J. A., Monni, S., Doering, U., Petrescu, A. M. R., Solazzo, E., and Oreggioni, G. D.: EDGAR v4.3.2 Global Atlas of the Three Major Greenhouse Gas Emissions for the Period 1970–2012, Earth System Science Data, 11, 959–1002, https://doi.org/10.5194/essd-11-959-2019, 2019.

Jensen, K. and Mcdonald, K.: Surface Water Microwave Product Series Version 3: A Near-Real Time and 25-Year Historical Global Inundated Area Fraction Time Series From Active and Passive Microwave Remote Sensing, IEEE Geoscience and Remote Sensing Letters, 16, 1402–1406, https://doi.org/10.1109/LGRS.2019.2898779, 2019.

Kouki, K., Luojus, K., and Riihelä, A.: Evaluation of Snow Cover Properties in ERA5 and ERA5-Land with Several Satellite-Based Datasets in the Northern Hemisphere in Spring 1982–2018, The Cryosphere, 17, 5007–5026, https://doi.org/10.5194/tc-17-5007-2023, 2023.

Laborte, A. G., Gutierrez, M. A., Balanza, J. G., Saito, K., Zwart, S. J., Boschetti, M., Murty, M., Villano, L., Aunario, J. K., Reinke, R., Koo, J., Hijmans, R. J., and Nelson, A.: RiceAtlas, a Spatial Database of Global Rice Calendars and Production, Scientific Data, 4, 170 074, https://doi.org/10.1038/sdata.2017.74, 2017.

Lan, X., K.W., T., and E.J., D.: Trends in globally-averaged CH4, N2O, and SF6 determined from NOAA Global Monitoring Laboratory measurements, https://doi.org/10.15138/P8XG-AA10, 2024.

Lehner, B. and Döll, P.: Development and Validation of a Global Database of Lakes, Reservoirs and Wetlands, Journal of Hydrology, 296, 1–22, https://doi.org/10.1016/j.jhydrol.2004.03.028, 2004.

Lehner, B., Anand, M., Fluet-Chouinard, E., Tan, F., Aires, F., Allen, G. H., Bousquet, P., Canadell, J. G., Davidson, N., Finlayson, C. M., Gumbricht, T., Hilarides, L., Hugelius, G., Jackson, R. B., Korver, M. C., McIntyre, P. B., Nagy, S., Olefeldt, D., Pavelsky, T. M., Pekel, J.-F., Poulter, B., Prigent, C., Wang, J., Worthington, T. A., Yamazaki, D., and Thieme, M.: Mapping the world's inland surface waters: an update to the Global Lakes and Wetlands Database (GLWD v2), Earth System Science Data Discussions, 2024, 1–49, https://doi.org/10.5194/essd-2024-204, 2024a.

Lehner, B., Beames, P., Mulligan, M., Zarfl, C., De Felice, L., Van Soesbergen, A., Thieme, M., Garcia De Leaniz, C., Anand, M., Belletti, B., Brauman, K. A., Januchowski-Hartley, S. R., Lyon, K., Mandle, L., Mazany-Wright, N., Messager, M. L., Pavelsky, T., Pekel, J.-F., Wang, J., Wen, Q., Wishart, M., Xing, T., Yang, X., and Higgins, J.: The Global Dam Watch Database of River Barrier and Reservoir Information for Large-Scale Applications, Scientific Data, 11, 1069, https://doi.org/10.1038/s41597-024-03752-9, 2024b.

Linke, S., Lehner, B., Ouellet Dallaire, C., Ariwi, J., Grill, G., Anand, M., Beames, P., Burchard-Levine, V., Maxwell, S., Moidu, H., Tan, F., and Thieme, M.: Global Hydro-Environmental Sub-Basin and River Reach Characteristics at High Spatial Resolution, Scientific Data, 6, 283, https://doi.org/10.1038/s41597-019-0300-6, 2019.

Lourenco, M., Fitchett, J. M., and Woodborne, S.: Peat Definitions: A Critical Review, Progress in Physical Geography: Earth and Environment, 47, 506–520, https://doi.org/10.1177/03091333221118353, 2023.

Loveland, T. R., Reed, B. C., Brown, J. F., Ohlen, D. O., Zhu, Z., Yang, L., and Merchant, J. W.: Development of a Global Land Cover Characteristics Database and IGBP DISCover from 1 Km AVHRR Data, International Journal of Remote Sensing, 21, 1303–1330, https://doi.org/10.1080/014311600210191, 2000.

Maclean, J., Hardy, B., and Hettel, G.: Rice Almanac, 4th edition: Source book for one of the most important economic activities on earth, IRRI, 2013.

Mastepanov, M., Sigsgaard, C., Dlugokencky, E. J., Houweling, S., Ström, L., Tamstorf, M. P., and Christensen, T. R.: Large Tundra Methane Burst during Onset of Freezing, Nature, 456, 628–630, https://doi.org/10.1038/nature07464, 2008.

Matthews, E. and Fung, I.: Methane Emission from Natural Wetlands: Global Distribution, Area, and Environmental Characteristics of Sources, Global Biogeochemical Cycles, 1, 61–86, https://doi.org/10.1029/GB001i001p00061, 1987.

McNicol, G., Fluet-Chouinard, E., Ouyang, Z., Knox, S., Zhang, Z., Aalto, T., Bansal, S., Chang, K.-Y., Chen, M., Delwiche, K., Feron, S., Goeckede, M., Liu, J., Malhotra, A., Melton, J. R., Riley, W., Vargas, R., Yuan, K., Ying, Q., Zhu, Q., Alekseychik, P., Aurela, M., Billesbach, D. P., Campbell, D. I., Chen, J., Chu, H., Desai, A. R., Euskirchen, E., Goodrich, J., Griffis, T., Helbig, M., Hirano, T., Iwata, H., Jurasinski, G., King, J., Koebsch, F., Kolka, R., Krauss, K., Lohila, A., Mammarella, I., Nilson, M., Noormets, A., Oechel, W., Peichl, M., Sachs, T., Sakabe, A., Schulze, C., Sonnentag, O., Sullivan, R. C., Tuittila, E.-S., Ueyama, M., Vesala, T., Ward, E., Wille, C., Wong, G. X., Zona, D., Windham-Myers, L., Poulter, B., and Jackson, R. B.: Upscaling Wetland Methane Emissions From the FLUXNET-CH4 Eddy Covariance Network (UpCH4 v1.0): Model Development, Network Assessment, and Budget Comparison, AGU Advances, 4, e2023AV000 956, https://doi.org/10.1029/2023AV000956, 2023.

Melton, J. R., Wania, R., Hodson, E. L., Poulter, B., Ringeval, B., Spahni, R., Bohn, T., Avis, C. A., Beerling, D. J., Chen, G., Eliseev, A. V., Denisov, S. N., Hopcroft, P. O., Lettenmaier, D. P., Riley, W. J., Singarayer, J. S., Subin, Z. M., Tian, H., Zürcher, S., Brovkin, V., van Bodegom, P. M., Kleinen, T., Yu, Z. C., and Kaplan, J. O.: Present State of Global Wetland Extent and Wetland Methane Modelling: Conclusions from a Model Inter-Comparison Project (WETCHIMP), Biogeosciences, 10, 753–788, https://doi.org/10.5194/bg-10-753-2013, 2013.

Messager, M. L., Lehner, B., Grill, G., Nedeva, I., and Schmitt, O.: Estimating the Volume and Age of Water Stored in Global Lakes Using a Geo-Statistical Approach, Nature Communications, 7, 13 603, https://doi.org/10.1038/ncomms13603, 2016.

Neeck, S. P., Lindstrom, E. J., Vaze, P. V., and Fu, L.-L.: Surface Water and Ocean Topography (SWOT) Mission, in: SPIE Remote Sensing, edited by Meynart, R., Neeck, S. P., and Shimoda, H., p. 85330G, Edinburgh, United Kingdom, https://doi.org/10.1117/12.981151, 2012.

Nisbet, E. G., Dlugokencky, E. J., Manning, M. R., Lowry, D., Fisher, R. E., France, J. L., Michel, S. E., Miller, J. B., White, J. W. C., Vaughn, B., Bousquet, P., Pyle, J. A., Warwick, N. J., Cain, M., Brownlow, R., Zazzeri, G., Lanoisellé, M., Manning, A. C., Gloor, E., Worthy, D. E. J., Brunke, E.-G., Labuschagne, C., Wolff, E. W., and Ganesan, A. L.: Rising Atmospheric Methane: 2007–2014 Growth and Isotopic Shift, Global Biogeochemical Cycles, 30, 1356–1370, https://doi.org/10.1002/2016GB005406, 2016.

Nisbet, E. G., Manning, M. R., Dlugokencky, E. J., Fisher, R. E., Lowry, D., Michel, S. E., Myhre, C. L., Platt, S. M., Allen, G., Bousquet, P., Brownlow, R., Cain, M., France, J. L., Hermansen, O., Hossaini, R., Jones, A. E., Levin, I., Manning, A. C., Myhre, G., Pyle, J. A., Vaughn, B. H., Warwick, N. J., and White, J. W. C.: Very Strong Atmospheric Methane Growth in the 4 Years 2014–2017: Implications for the Paris Agreement, Global Biogeochemical Cycles, 33, 318–342, https://doi.org/10.1029/2018GB006009, 2019.

Normandin, C., Frappart, F., Lubac, B., Bélanger, S., Marieu, V., Blarel, F., Robinet, A., and Guiastrennec-Faugas, L.: Quantification of Surface Water Volume Changes in the Mackenzie Delta Using Satellite Multi-Mission Data, Hydrology and Earth System Sciences, 22, 1543–1561, https://doi.org/10.5194/hess-22-1543-2018, 2018.

Normandin, C., Frappart, F., Bourrel, L., Diepkilé, A. T., Mougin, E., Zwarts, L., Blarel, F., Egon, F., and Wigneron, J.-P.: Quantification of Surface Water Extent and Volume in the Inner Niger Delta (IND) over 2000–2022 Using Multispectral Imagery and Radar Altimetry, Geocarto International, 39, 2311 203, https://doi.org/10.1080/10106049.2024.2311203, 2024.

Obled, C. and Zin, I.: TOPMODEL : principes de fonctionnement et application, La Houille Blanche, 90, 65–77, https://doi.org/10.1051/lhb:200401009, 2004.

Olefeldt, D., Hovemyr, M., Kuhn, M., Bastviken, D., Bohn, T., Connolly, J., Crill, P., Euskirchen, E., Finkelstein, S., Genet, H., Grosse, G., Harris, L., Heffernan, L., Helbig, M., Hugelius, G., Hutchins, R., Juutinen, S., Lara, M., Malhotra, A., Manies, K., McGuire, D., Natali, S., O'Donnell, J., Parmentier, F.-J., Räsänen, A., Schädel, C., Sonnentag, O., Strack, M., Tank, S., Treat, C., Varner, R., Virtanen, T., Warren, R., and Watts, J.: The fractional land cover estimates from the Boreal-Arctic Wetland and Lake Dataset (BAWLD), 2021., https://doi.org/10.18739/A2C824F9X, 2021a.

Olefeldt, D., Hovemyr, M., Kuhn, M. A., Bastviken, D., Bohn, T. J., Connolly, J., Crill, P., Euskirchen, E. S., Finkelstein, S. A., Genet, H., Grosse, G., Harris, L. I., Heffernan, L., Helbig, M., Hugelius, G., Hutchins, R., Juutinen, S., Lara, M. J., Malhotra, A., Manies, K., McGuire, A. D., Natali, S. M., O'Donnell, J. A., Parmentier, F.-J. W., Räsänen, A., Schädel, C., Sonnentag, O., Strack, M., Tank, S. E., Treat, C., Varner, R. K., Virtanen, T., Warren, R. K., and Watts, J. D.: The Boreal–Arctic Wetland and Lake Dataset (BAWLD), Earth System Science Data, 13, 5127–5149, https://doi.org/10.5194/essd-13-5127-2021, 2021b.

Pangala, S. R., Enrich-Prast, A., Basso, L. S., Peixoto, R. B., Bastviken, D., Hornibrook, E. R. C., Gatti, L. V., Marotta, H., Calazans, L. S. B., Sakuragui, C. M., Bastos, W. R., Malm, O., Gloor, E., Miller, J. B., and Gauci, V.: Large Emissions from Floodplain Trees Close the Amazon Methane Budget, Nature, 552, 230–234, https://doi.org/10.1038/nature24639, 2017.

Papa, F., Prigent, C., Durand, F., and Rossow, W. B.: Wetland Dynamics Using a Suite of Satellite Observations: A Case Study of Application and Evaluation for the Indian Subcontinent, Geophysical Research Letters, 33, 2006GL025 767, https://doi.org/10.1029/2006GL025767, 2006.

Papa, F., Güntner, A., Frappart, F., Prigent, C., and Rossow, W. B.: Variations of Surface Water Extent and Water Storage in Large River Basins: A Comparison of Different Global Data Sources, Geophysical Research Letters, 35, 2008GL033 857, https://doi.org/10.1029/2008GL033857, 2008.

Papa, F., Prigent, C., Aires, F., Jimenez, C., Rossow, W. B., and Matthews, E.: Interannual Variability of Surface Water Extent at the Global Scale, 1993–2004, Journal of Geophysical Research: Atmospheres, 115, 2009JD012 674, https://doi.org/10.1029/2009JD012674, 2010.

Pedinotti, V., Boone, A., Ricci, S., Biancamaria, S., and Mognard, N.: Assimilation of Satellite Data to Optimize Large-Scale Hydrological Model Parameters: A Case Study for the SWOT Mission, Hydrology and Earth System Sciences, 18, 4485–4507, https://doi.org/10.5194/hess-18-4485-2014, 2014.

Pekel, J.-F., Cottam, A., Gorelick, N., and Belward, A. S.: High-Resolution Mapping of Global Surface Water and Its Long-Term Changes, Nature, 540, 418–422, https://doi.org/10.1038/nature20584, 2016.

Peltola, O., Vesala, T., Gao, Y., Räty, O., Alekseychik, P., Aurela, M., Chojnicki, B., Desai, A. R., Dolman, A. J., Euskirchen, E. S., Friborg, T., Göckede, M., Helbig, M., Humphreys, E., Jackson, R. B., Jocher, G., Joos, F., Klatt, J., Knox, S. H., Kowalska, N., Kutzbach, L., Lienert, S., Lohila, A., Mammarella, I., Nadeau, D. F., Nilsson, M. B., Oechel, W. C., Peichl, M., Pypker, T., Quinton, W., Rinne, J., Sachs, T., Samson, M., Schmid, H. P., Sonnentag, O., Wille, C., Zona, D., and Aalto, T.: Monthly Gridded Data Product of Northern Wetland Methane Emissions Based on Upscaling Eddy Covariance Observations, Earth System Science Data, 11, 1263–1289, https://doi.org/10.5194/essd-11-1263-2019, 2019.

Peral, E. and Esteban-Fernandez, D.: Swot Mission Performance and Error Budget, in: IGARSS 2018 - 2018 IEEE International Geoscience and Remote Sensing Symposium, pp. 8625–8628, IEEE, Valencia, ISBN 978-1-5386-7150-4, https://doi.org/10.1109/IGARSS.2018.8517385, 2018.

Pham-Duc, B., Prigent, C., Aires, F., and Papa, F.: Comparisons of Global Terrestrial Surface Water Datasets over 15 Years, Journal of Hydrometeorology, 18, 993–1007, https://doi.org/10.1175/JHM-D-16-0206.1, 2017.

Portmann, F. T., Siebert, S., and Döll, P.: MIRCA2000-Global Monthly Irrigated and Rainfed Crop Areas around the Year 2000: A New High-Resolution Data Set for Agricultural and Hydrological Modeling: MONTHLY IRRIGATED AND RAINFED CROP AREAS, Global Biogeochemical Cycles, 24, n/a–n/a, https://doi.org/10.1029/2008GB003435, 2010.

Poulter, B., Bousquet, P., Canadell, J. G., Ciais, P., Peregon, A., Saunois, M., Arora, V. K., Beerling, D. J., Brovkin, V., Jones, C. D., Joos, F., Gedney, N., Ito, A., Kleinen, T., Koven, C. D., McDonald, K., Melton, J. R., Peng, C., Peng, S., Prigent, C., Schroeder, R., Riley, W. J., Saito, M., Spahni, R., Tian, H., Taylor, L., Viovy, N., Wilton, D., Wiltshire, A., Xu, X., Zhang, B., Zhang, Z., and Zhu, Q.: Global Wetland Contribution to 2000–2012 Atmospheric Methane Growth Rate Dynamics, Environmental Research Letters, 12, 094 013, https://doi.org/10.1088/1748-9326/aa8391, 2017.

Prigent, C., Matthews, E., Aires, F., and Rossow, W. B.: Remote Sensing of Global Wetland Dynamics with Multiple Satellite Data Sets, Geophysical Research Letters, 28, 4631–4634, https://doi.org/10.1029/2001GL013263, 2001.

Prigent, C., Papa, F., Aires, F., Rossow, W. B., and Matthews, E.: Global Inundation Dynamics Inferred from Multiple Satellite Observations, 1993–2000, Journal of Geophysical Research, 112, D12 107, https://doi.org/10.1029/2006JD007847, 2007.

Prigent, C., Lettenmaier, D. P., Aires, F., and Papa, F.: Toward a High-Resolution Monitoring of Continental Surface Water Extent and Dynamics, at Global Scale: From GIEMS (Global Inundation Extent from Multi-Satellites) to SWOT (Surface Water Ocean Topography), Surveys in Geophysics, 37, 339–355, https://doi.org/10.1007/s10712-015-9339-x, 2016.

Prigent, C., Jimenez, C., and Bousquet, P.: Satellite-Derived Global Surface Water Extent and Dynamics Over the Last 25 Years (GIEMS-2), Journal of Geophysical Research: Atmospheres, 125, https://doi.org/10.1029/2019JD030711, 2020.

Ringeval, B., Decharme, B., Piao, S. L., Ciais, P., Papa, F., de Noblet-Ducoudré, N., Prigent, C., Friedlingstein, P., Gouttevin, I., Koven, C., and Ducharne, A.: Modelling Sub-Grid Wetland in the ORCHIDEE Global Land Surface Model: Evaluation against River Discharges and Remotely Sensed Data, Geoscientific Model Development, 5, 941–962, https://doi.org/10.5194/gmd-5-941-2012, 2012.

Rosenqvist, J., Rosenqvist, A., Jensen, K., and McDonald, K.: Mapping of Maximum and Minimum Inundation Extents in the Amazon Basin 2014–2017 with ALOS-2 PALSAR-2 ScanSAR Time-Series Data, Remote Sensing, 12, 1326, https://doi.org/10.3390/rs12081326, 2020.

Rößger, N., Sachs, T., Wille, C., Boike, J., and Kutzbach, L.: Seasonal Increase of Methane Emissions Linked to Warming in Siberian Tundra, Nature Climate Change, 12, 1031–1036, https://doi.org/10.1038/s41558-022-01512-4, 2022.

Salmon, J., Friedl, M. A., Frolking, S., Wisser, D., and Douglas, E. M.: Global Rain-Fed, Irrigated, and Paddy Croplands: A New High Resolution Map Derived from Remote Sensing, Crop Inventories and Climate Data, International Journal of Applied Earth Observation and Geoinformation, 38, 321–334, https://doi.org/10.1016/j.jag.2015.01.014, 2015.

Saunois, M., Stavert, A. R., Poulter, B., Bousquet, P., Canadell, J. G., Jackson, R. B., Raymond, P. A., Dlugokencky, E. J., Houweling, S., Patra, P. K., Ciais, P., Arora, V. K., Bastviken, D., Bergamaschi, P., Blake, D. R., Brailsford, G., Bruhwiler, L., Carlson, K. M., Carrol, M., Castaldi, S., Chandra, N., Crevoisier, C., Crill, P. M., Covey, K., Curry, C. L., Etiope, G., Frankenberg, C., Gedney, N., Hegglin, M. I., Höglund-Isaksson, L., Hugelius, G., Ishizawa, M., Ito, A., Janssens-Maenhout, G., Jensen, K. M., Joos, F., Kleinen, T., Krummel, P. B., Langenfelds, R. L., Laruelle, G. G., Liu, L., Machida, T., Maksyutov, S., McDonald, K. C., McNorton, J., Miller, P. A., Melton, J. R., Morino, I., Müller, J., Murguia-Flores, F., Naik, V., Niwa, Y., Noce, S., O'Doherty, S., Parker, R. J., Peng, C., Peng, S., Peters, G. P., Prigent, C., Prinn, R., Ramonet, M., Regnier, P., Riley, W. J., Rosentreter, J. A., Segers, A., Simpson, I. J., Shi, H., Smith, S. J., Steele, L. P., Thornton, B. F., Tian, H., Tohjima, Y., Tubiello, F. N., Tsuruta, A., Viovy, N., Voulgarakis, A., Weber, T. S., van Weele, M., van der Werf, G. R., Weiss, R. F., Worthy, D., Wunch, D., Yin, Y., Yoshida, Y., Zhang, W., Zhang, Z., Zhao, Y., Zheng, B., Zhu, Q., Zhu, Q., and Zhuang, Q.: The Global Methane Budget 2000–2017, Earth System Science Data, 12, 1561–1623, https://doi.org/10.5194/essd-12-1561-2020, 2020.

Saunois, M., Martinez, A., Poulter, B., Zhang, Z., Raymond, P., Regnier, P., Canadell, J. G., Jackson, R. B., Patra, P. K., Bousquet, P., Ciais, P., Dlugokencky, E. J., Lan, X., Allen, G. H., Bastviken, D., Beerling, D. J., Belikov, D. A., Blake, D. R., Castaldi, S., Crippa, M., Deemer, B. R., Dennison, F., Etiope, G., Gedney, N., Höglund-Isaksson, L., Holgerson, M. A., Hopcroft, P. O., Hugelius, G., Ito, A., Jain, A. K., Janardanan, R., Johnson, M. S., Kleinen, T., Krummel, P., Lauerwald, R., Li, T., Liu, X., McDonald, K. C., Melton, J. R., Mühle, J., Müller, J., Murguia-Flores, F., Niwa, Y., Noce, S., Pan, S., Parker, R. J., Peng, C., Ramonet, M., Riley, W. J., Rocher-Ros, G., Rosentreter, J. A., Sasakawa, M., Segers, A., Smith, S. J., Stanley, E. H., Thanwerdas, J., Tian, H., Tsuruta, A., Tubiello, F. N., Weber, T. S., Van Der Werf, G., Worthy, D. E., Xi, Y., Yoshida, Y., Zhang, W., Zheng, B., Zhu, Q., Zhu, Q., and Zhuang, Q.: Global Methane Budget 2000–2020, https://doi.org/10.5194/essd-2024-115, 2024.

Schroeder, R., McDonald, K., Chapman, B., Jensen, K., Podest, E., Tessler, Z., Bohn, T., and Zimmermann, R.: Development and Evaluation of a Multi-Year Fractional Surface Water Data Set Derived from Active/Passive Microwave Remote Sensing Data, Remote Sensing, 7, 16 688–16 732, https://doi.org/10.3390/rs71215843, 2015.

Szopa, S., Naik, V., Adhikary, B., Artaxo, P., Berntsen, T., Collins, W., Fuzzi, S., Gallardo, L., Kiendler-Scharr, A., Klimont, Z., Liao, H., Unger, N., and Zanis, P.: Short-Lived Climate Forcers, in: Climate Change 2021: The Physical Science Basis. Contribution of Working Group I to the Sixth Assessment Report of the Intergovernmental Panel on Climate Change, edited by Masson-Delmotte, V., Zhai, P., Pirani, A., Connors, S. L., Péan, C., Berger, S., Caud, N., Chen, Y., Goldfarb, L., Gomis, M. I., Huang, M., Leitzell, K., Lonnoy, E., Matthews, J. B. R., Maycock, T. K., Waterfield, T., Yelekçi, O., Yu, R., and Zhou, B., book section 6, Cambridge University Press, Cambridge, UK and New York, NY, USA, https://doi.org/10.1017/9781009157896.008, 2021.

Thornton, B. F., Wik, M., and Crill, P. M.: Double-counting Challenges the Accuracy of High-latitude Methane Inventories, Geophysical Research Letters, 43, https://doi.org/10.1002/2016GL071772, 2016.

Tootchi, A., Jost, A., and Ducharne, A.: Multi-Source Global Wetland Maps Combining Surface Water Imagery and Groundwater Constraints, Earth System Science Data, 2019.

Tuanmu, M.-N. and Jetz, W.: A Global 1-km Consensus Land-cover Product for Biodiversity and Ecosystem Modelling, Global Ecology and Biogeography, 23, 1031–1045, https://doi.org/10.1111/geb.12182, 2014.

Vanin, F., Laberinti, P., Donlon, C., Fiorelli, B., Barat, I., Sole, M. P., Palladino, M., Eggers, P., Rudolph, T., and Galeazzi, C.: Copernicus Imaging Microwave Radiometer (CIMR): System Aspects and Technological Challenges, in: IGARSS 2020 - 2020 IEEE International Geoscience and Remote Sensing Symposium, pp. 6535–6538, IEEE, Waikoloa, HI, USA, ISBN 978-1-72816-374-1, https://doi.org/10.1109/IGARSS39084.2020.9324259, 2020.

Vroom, R., Van Den Berg, M., Pangala, S., Van Der Scheer, O., and Sorrell, B.: Physiological Processes Affecting Methane Transport by Wetland Vegetation – A Review, Aquatic Botany, 182, 103 547, https://doi.org/10.1016/j.aquabot.2022.103547, 2022.

Wania, R., Melton, J. R., Hodson, E. L., Poulter, B., Ringeval, B., Spahni, R., Bohn, T., Avis, C. A., Chen, G., Eliseev, A. V., Hopcroft, P. O., Riley, W. J., Subin, Z. M., Tian, H., van Bodegom, P. M., Kleinen, T., Yu, Z. C., Singarayer, J. S., Zürcher, S., Lettenmaier, D. P., Beerling, D. J., Denisov, S. N., Prigent, C., Papa, F., and Kaplan, J. O.: Present State of Global Wetland Extent and Wetland Methane Modelling: Methodology of a Model Inter-Comparison Project (WETCHIMP), Geoscientific Model Development, 6, 617–641, https://doi.org/10.5194/gmd-6-617-2013, 2013.

Widhalm, B., Bartsch, A., and Heim, B.: A Novel Approach for the Characterization of Tundra Wetland Regions with C-band SAR Satellite Data, International Journal of Remote Sensing, 36, 5537–5556, https://doi.org/10.1080/01431161.2015.1101505, 2015.

Xi, Y., Peng, S., Ducharne, A., Ciais, P., Gumbricht, T., Jimenez, C., Poulter, B., Prigent, C., Qiu, C., Saunois, M., and Zhang, Z.: Gridded Maps of Wetlands Dynamics over Mid-Low Latitudes for 1980–2020 Based on TOPMODEL, Scientific Data, 9, 347, https://doi.org/10.1038/s41597-022-01460-w, 2022.

Xu, J., Morris, P. J., Liu, J., and Holden, J.: PEATMAP: Refining Estimates of Global Peatland Distribution Based on a Meta-Analysis, CATENA, 160, 134–140, https://doi.org/10.1016/j.catena.2017.09.010, 2018.

Zeiger, P., Frappart, F., Darrozes, J., Prigent, C., Jiménez, C., and Bourrel, L.: Weekly Mapping of Surface Water Extent in the Intertropical Wetlands Using Spaceborne GNSS Reflectometry, Journal of Hydrology, 626, 130 305, https://doi.org/10.1016/j.jhydrol.2023.130305, 2023.

Zhang, B., Tian, H., Lu, C., Chen, G., Pan, S., Anderson, C., and Poulter, B.: Methane Emissions from Global Wetlands: An Assessment of the Uncertainty Associated with Various Wetland Extent Data Sets, Atmospheric Environment, 165, 310–321, https://doi.org/10.1016/j.atmosenv.2017.07.001, 2017.

Zhang, Z., Fluet-Chouinard, E., Jensen, K., McDonald, K., Hugelius, G., Gumbricht, T., Carroll, M., Prigent, C., Bartsch,
850   A., and Poulter, B.: Development of a global dataset of Wetland Area and Dynamics for Methane Modeling (WAD2M),
       https://doi.org/10.5281/zenodo.5553187, 2021a.

Zhang, Z., Fluet-Chouinard, E., Jensen, K., McDonald, K., Hugelius, G., Gumbricht, T., Carroll, M., Prigent, C., Bartsch, A., and Poulter,
       B.: Development of the Global Dataset of Wetland Area and Dynamics for Methane Modeling (WAD2M), Earth System Science Data,
       13, 2001–2023, https://doi.org/10.5194/essd-13-2001-2021, 2021b.

855   Zhang, Z., Poulter, B., Feldman, A. F., Ying, Q., Ciais, P., Peng, S., and Li, X.: Recent Intensification of Wetland Methane Feedback, Nature
       Climate Change, 13, 430–433, https://doi.org/10.1038/s41558-023-01629-0, 2023.

Zona, D., Gioli, B., Commane, R., Lindaas, J., Wofsy, S. C., Miller, C. E., Dinardo, S. J., Dengel, S., Sweeney, C., Karion, A., Chang, R.
       Y.-W., Henderson, J. M., Murphy, P. C., Goodrich, J. P., Moreaux, V., Liljedahl, A., Watts, J. D., Kimball, J. S., Lipson, D. A., and Oechel,
       W. C.: Cold Season Emissions Dominate the Arctic Tundra Methane Budget, Proceedings of the National Academy of Sciences, 113,
860   40–45, https://doi.org/10.1073/pnas.1516017113, 2016.